

1 **Physical processes influencing the Asian climate due to black carbon emission**
2 **over East and South Asia**

3 *Feifei Luo¹, Bjørn H. Samset², Camilla W. Stjern², Manoj Joshi³, Laura J. Wilcox⁴,*
4 *Robert J. Allen⁵, Wei Hua¹, and Shuanglin Li^{6,7}*

5 1. School of Atmospheric Sciences/Plateau Atmosphere and Environment Key
6 Laboratory of Sichuan Province/Meteorological Disaster Prediction and Warning
7 Engineering Laboratory of Sichuan Province, Chengdu University of Information
8 Technology, Chengdu, China

9 2. CICERO Center for International Climate Research, Oslo, Norway

10 3. Climatic Research Unit, School of Environmental Sciences, University of East
11 Anglia, Norwich, United Kingdom

12 4. National Centre for Atmospheric Science, University of Reading, Reading, United
13 Kingdom

14 5. Department of Earth and Planetary Sciences, University of California Riverside,
15 Riverside, CA, United States of America

16 6. Climate Change Research Center, Institute of Atmospheric Physics, Chinese
17 Academy of Sciences, Beijing, China

18 7. Department of Atmospheric Science, China University of Geoscience, Wuhan,
19 China

20 Corresponding author: Feifei Luo (lff@cuit.edu.cn)

21 To be submitted to Atmospheric Chemistry and Physics

22

Abstract

Many studies have shown that black carbon (BC) aerosols over Asia have significant impacts on regional climate, but with large diversities in intensity, spatial distribution and physical mechanism of regional responses. In this study, we utilized a set of Systematic Regional Aerosol Perturbations (SyRAP) using a reduced complexity climate model, FORTE2, to investigate responses of the Asian climate to BC aerosols over East Asia only, South Asia only, and both regions at once, and thoroughly examine related physical processes. Results show that regional BC aerosols lead to a strong surface cooling, air temperature warming in the low-level troposphere, and drying over the perturbed areas, with seasonal differences in magnitude and spatial distribution. Atmospheric energy budget analysis suggests that reductions in local precipitation primarily depend on the substantial local atmospheric heating due to shortwave absorption by BC. Increases in dry static energy (DSE) flux divergence partly offset the reduced precipitation over north China in summer and most of China and India in the other three seasons. Decreases in DSE flux divergence lead to stronger reduction in precipitation over south China and central India in summer. Changes in DSE flux divergence are mainly due to vertical motions driven by diabatic heating in the middle and lower troposphere. BC perturbations also exert non-local climate impacts through the changes in DSE flux divergence. This study provides a full chain of physical processes of the local climate responses to the Asian BC increases, and gives some insights to better understand the uncertainties of model responses.

1. Introduction

Black carbon (BC) aerosol, a short-lived pollutant and climate forcer, is emitted from the incomplete combustion of biomass and fossil fuels, and exerts significant effects on global and regional climate (Ramanathan and Carmichael, 2008; Bond et al., 2013; Stjern et al., 2017; IPCC, 2021; Li et al., 2022). Alongside rapid economic developments of China and India over the past few decades, East and South Asia have become the highest BC emissions hotspots in the world. Despite BC emissions from China decreasing substantially in the past decade, East and South Asia are expected to remain the highest BC loadings globally in the coming decades (Lund et al., 2019). Hence, the climate impacts of BC emissions from East and South Asia have been extensively investigated (e.g. Li et al., 2016; Lou et al., 2019; Xie et al., 2020; Westervelt et al., 2020; Herbert et al., 2022; Yang et al., 2022). Although many model studies have shown that Asian BC aerosols are of great importance for local climate (especially the Asian monsoonal systems), considerable uncertainty exists regarding the intensity and spatial distribution of the Asian climate responses to BC forcings, as well as the related physical mechanisms.

Menon et al. (2002) found that during summer, a large BC forcing induced a “southern flooding and northern drought” precipitation pattern in China based on a global climate model (CGCM). In contrast, some subsequent modeling studies found that BC forcing acted to suppress precipitation in southern and eastern China while strengthening it in the north (Gu et al., 2006; Zhang et al., 2009; Liu et al., 2018). Additionally, some studies suggested that BC aerosols caused a tripolar precipitation pattern with wetting-drying-wetting from north to south China (Mahmood and Li, 2014; Xie et al., 2020), or there was no statistically significant response in precipitation over East China (Jiang et al., 2013; Guo et al., 2013; Wang et al., 2017).

Regional precipitation responses to BC aerosols can be attributed to both surface cooling induced by aerosol-radiation interaction (ARI) and atmospheric heating by aerosol absorption (Stier et al., 2024). However, the relative importance of the two effects is debated. Persad et al. (2017) have shown that surface cooling dominates the reduction of the East Asian summer precipitation due to the decreased land-sea thermal

contrast, whilst atmospheric heating partially offset the reduction. Xie et al. (2020) have proposed that the precipitation responses mainly result from the upper-level atmospheric heating over Asia, which enhances the upper-level meridional land-sea thermal gradient and subsequently strengthens the low-level monsoon circulation.

Similarly, the South Asian summer monsoon (SASM) exhibits inconsistent responses to BC forcings. Some model studies suggested that increased BC aerosols can lead to a weakened SASM (Lau and Kim, 2007; Meehl et al., 2008), while others found that there should be a strengthened SASM via increasing the atmospheric meridional land-sea thermal gradient, or an elevated heat pump effect (Lau et al., 2006; Xie et al., 2020; Westervelt et al., 2020). Westervelt et al. (2018) conducted aerosol removal experiments using three CGCMs, and found that Indian BC decreases lead to no change or a small decrease in precipitation in India.

In addition, Jiang et al. (2017) found that BC forcing can lead to an intensification of the East Asian winter monsoon (EAWM) northern mode via heating Tibetan Plateau using the CAM5 model. On the contrary, Lou et al. (2019) suggested that BC emitted from the North China can weaken the EAWM through ocean, sea ice, and cloud feedbacks based on CESM. BC aerosol can also affect spring and autumn precipitation in China (Guo et al., 2013; Hu and Liu, 2014; Deng et al., 2014).

By comparing the sum of Asian climate responses to individual responses over East and South Asia with the responses to simultaneous forcing, the regional linearity of BC forcing has been investigated, but the results remain unclear. Chen et al. (2020) and Herbert et al. (2022) suggested that the responses were highly nonlinear due to interactions of atmospheric circulation changes, based on a regional climate model and an atmospheric general circulation model (AGCM), respectively. In contrast, Reccia and Lucarini (2023) and Stjern et al. (2024) found that the responses were almost linear in most of Asian regions. The difference may be related to the different spatial extent of the aerosol perturbation in the simulation design (Stjern et al., 2024).

These inconsistent results, and the large uncertainty in the simulated response of the Asian climate to BC changes, are partly related to differences in the modeling approach (e.g., AGCMs versus CGCMs/ESMs) and also the magnitude and location of

the BC perturbation. Atmosphere-only GCMs lack SST feedbacks, which are crucial in influencing the Asian monsoon (Dong et al., 2019), while CGCMs or ESMs involving more and more complex physical processes make it difficult to identify the key physical processes behind impacts of regional BC aerosols on Asian climate. The inconsistency may also be associated with model-specific differences. Different models that include different physical processes, combined with different experiment designs that can influence the atmospheric circulation response, make it challenging to understand the causes of differences between studies.

Hence, reduced complexity models, such as FORTE2 (Fast Ocean Rapid Troposphere Experiment version 2), provide an alternative and useful tool for such studies, given that such models not only include all the main mechanisms of aerosol-climate interactions, but also allow fast speed of integration and longer simulations with lower cost. Stjern et al. (2024) have utilized FORTE2 to perform a series of Systematic Regional Aerosol Perturbations (SyRAP) simulations, employing regionally realistic aerosol forcing for the period 2003-2021 from the Copernicus Atmosphere Monitoring Service (CAMS) reanalysis (Inness et al., 2019). The core simulations include: (1) baseline simulations forced by GHG concentrations at different climate states (i.e. pre-industrial, present-day and future CO₂ levels) and no aerosol; (2) perturbation simulations forced by added absorbing aerosols (BC, and organic carbon, OC) or scattering aerosols (sulfate, SO₄) over East Asia only, South Asia only, and over both regions simultaneously with only ARI effects, and GHG concentrations at different climate states; (3) Aerosol-cloud interactions (ACI) simulations forced by added SO₄ in the combined East Asia and South Asia region in which ACI were turned on. The SyRAP-FORTE2 framework enables comprehensive analysis of climate effects of different regional aerosol perturbations and aerosol species, as well as ARI versus ACI, and allows comparison of their relative importance and interactions (Stjern et al., 2024).

In this study, considering that BC aerosols mostly impact climate through ARI, we aim to address the following two questions focused on BC ARI effects, based on the simulations of the regional BC perturbations in SyRAP-FORTE2: (1) what are the responses of Asian climate to East Asian BC perturbations, South Asian BC

perturbations, or both regions simultaneously, respectively? (2) What are the key physical processes involved in these responses?

The rest of the paper is organized as follows: section 2 describes the FORTE2 model, SyRAP simulations, and analysis methods and datasets; section 3 briefly evaluates the climatology of SyRAP simulations, examines responses to the regional BC perturbations in SyRAP-FORTE2, and investigates the underlying physical processes; section 4 compares the results of the atmospheric energy budget in SyRAP-FORTE2 with those in the PDRMIP models; Finally, the summary and discussion are provided in section 5.

2. Methods

2.1 The FORTE2 model

FORTE2 is an intermediate-complexity coupled atmosphere-ocean general circulation model (Blaker et al., 2021). The atmospheric component is the Intermediate General Circulation Model 4 (IGCM4) with a horizontal resolution of approximately 2.8° (T42), and 35 sigma levels extending up to 0.1 hPa (Joshi et al., 2015). IGCM4 includes schemes for radiation, land-surface properties, convection, precipitation, and clouds (Zhong and Haigh, 1995; Betts and Miller, 1993). The oceanic component is the Modular Ocean Model-Array (MOMA) with a horizontal grid spacing $2^\circ \times 2^\circ$, and 15 z-layer levels increasing in thickness with depth from 30 m at the surface to 800 m at the bottom (Webb, 1996). Sea ice is represented by a barrier to heat fluxes between the ocean and atmosphere components. FORTE2 runs without flux adjustments (Blaker et al., 2021). Blaker et al. (2021) have thoroughly evaluated FORTE2's skill in simulating the atmosphere, ocean and major climatic modes, suggesting that FORTE2 can satisfactorily simulate a climate state and climate variability.

2.2 Regional BC perturbation simulations in SyRAP-FORTE2

SyRAP-FORTE2 used the global gridded monthly aerosol optical depths (AOD) and vertical distributions from the CAMS reanalysis (CAMSRA) for 2003-2021 (Inness et al., 2019), rather than aerosol gas emissions/concentrations employed by most CMIP6 models. The CAMSRA incorporates anthropogenic BC emissions from the

MACCcity inventory (Granier et al., 2011) for 2003-2010, transitioning to Representative Concentration Pathway 8.5 emissions (Riahi et al., 2011) post-2010. The simulations were idealized with monthly AOD climatologies prescribed as repeating annual cycles. The regional annual mean BC AOD perturbation is about 0.015 for East China, and about 0.01 for India, respectively (Fig. S1). Aerosols were distributed vertically uniformly from the second lowest model layer (σ , or $p/p_{\text{surface}} = 0.88$ or approximately 950 m above the surface) up to a pressure level p_{min} . For each gridbox, p_{min} was derived from CAMSRA as either 850 hPa or the lowest pressure level where the 2003-2021 mean BC+OC+SO₄ mixing ratio falls below 5×10^9 kg/kg, whichever value is lower. In topographic regions, additional constraints require $\sigma_{\text{min}} < 0.75$ and $p_{\text{min}} > 300$ hPa. The seasonal changes of the regional mean p_{min} over China and India are illustrated in Figure S2. Aerosols are not transported in FORTE2. The application of aerosol distributions from a reanalysis means that the simulations include a realistic aerosol spatial distribution, but the lack of aerosol transport means that there are no feedbacks between the climate response and the aerosol distribution (e.g. increased precipitation leading to increased aerosol removal). For more details on aerosols implementation in FORTE2, see Stjern et al. (2024).

There is no significant difference in Asian climate responses to BC aerosols between the pre-industrial and present-day climate conditions in the SyRAP-FORTE2 simulations (Stjern et al., 2024). Hence, in this study the baseline simulation (piC) and the BC perturbation simulations of three different regions at the pre-industrial climate conditions (280 ppmv) were performed to explore potential physical processes of Asian BC aerosols influencing the local climate (Table 1). Given that BC primarily influences climate through direct scattering and absorption of radiation (Bond et al., 2013), only climate impacts due to ARI (including the semi-direct effect of BC) were considered here. All simulations were run for 200 years, with years 51-200 used for analysis.

2.3 Analysis methods and Datasets

The response to a particular regional forcing is estimated by the mean difference between the perturbation simulation and the baseline simulation. Statistical significance

of the response is assessed using a two-tailed Student's t-test.

The atmospheric energy budget is applied to understand the precipitation responses (Muller and O’Gorman, 2011; Richardson et al., 2016; Liu et al., 2018). The energy associated with precipitation can be separated into a thermodynamic component with only changes in diabatic cooling (Q), and a dynamic component with only changes in dry static energy (DSE) flux divergence (H), as shown in Eq. (1):

$$L_c \delta P = \delta Q + \delta H \quad (1)$$

where L_c is the latent heat of condensation, P is precipitation, δ denotes a perturbation. Then,

$$\delta Q = \delta LWC - \delta SWA - \delta SH \quad (2)$$

where LWC is atmospheric longwave cooling, SWA is atmospheric shortwave absorption, and SH is sensible heat flux from the surface.

δH is calculated as a residual between $L_c \delta P$ and δQ . Furthermore, H can be seen as the sum of the changes in mean (H_m) and eddy (H_{trans}) components. δH_m can be decomposed into four components associated with dynamic and thermodynamic effects on vertical and horizontal advection of DSE, as shown in Eq. (3):

$$\begin{aligned} \delta H_m &= \delta H_{Dyn_v} + \delta H_{Thermo_v} + \delta H_{Dyn_h} + \delta H_{Thermo_h} \\ &= \int \delta \bar{\omega} \frac{\partial \bar{s}}{\partial p} \frac{dp}{g} + \int \bar{\omega} \delta \left(\frac{\partial \bar{s}}{\partial p} \right) \frac{dp}{g} + \int \delta \bar{u} \cdot \nabla \bar{s} \frac{dp}{g} + \int \bar{u} \cdot \delta (\nabla \bar{s}) \frac{dp}{g} \quad (3) \end{aligned}$$

where ω is vertical velocity, s is DSE, p is pressure, g is the gravitational acceleration, u is horizontal wind vector, ∇ is the horizontal gradient, and an overbar indicates climatological monthly means. Therefore, H_{Dyn_v} is related to changes in vertical velocity, H_{Thermo_v} is related to changes in vertical DSE gradients, H_{Dyn_h} is related to changes in horizontal winds, and H_{Thermo_h} is related to changes in horizontal DSE gradients. δH_{trans} is calculated as a residual between δH and δH_m .

To evaluate the skill of FORTE2 to simulate observed climate variables, monthly precipitation, surface temperature (T_s), and horizontal wind components were used from the NOAA-CIRES-DOE 20th Century Reanalysis V3 (20CR) on a $2^\circ \times 2^\circ$ grid spanning 1806 to 2015 (Compo et al., 2011). The 20CR is only based on surface observations of synoptic pressure of NOAA’s physical Sciences Laboratory. Monthly

sea level pressure (SLP) data were from the Hadley Centre (HadSLP) in a horizontal resolution of $5^\circ \times 5^\circ$ (Allan & Ansell, 2006).

To compare the response of FORTE2 to BC perturbations with those of CMIP class models, we used the PDRMIP 10 times the modern Asian BC concentrations/emissions perturbation simulations, and their corresponding baseline simulations with modern aerosol concentrations/emissions and greenhouse gases under year-2000 conditions, from the 5 GCMs (CESM1-CAM5, GISS-E2-R, HadGEM3, MIROC, and NorESM1; Table S1). More details of the PDRMIP design can be found in Myhre et al. (2017), and an overview of the Asian monsoon response is given in Liu et al. (2018).

3. Results

3.1 Evaluation of baseline climate in SyRAP-FORTE2

Blaker et al. (2021) present a detailed overview of the FORTE2 climatology. The model simulates the Asian climate well, and the more focused evaluation presented by Stjern et al. (2024) demonstrates that FORTE2 is an appropriate tool to study the effects of local aerosol perturbations on Asian climate. Here, for completeness, we assess an overview of the skill of FORTE2 in simulating the Asian climate. The seasonal evolutions of precipitation and surface temperature (T_s) in East China and India, and the climatology of lower tropospheric circulation (SLP and 850 hPa horizontal wind) in the baseline experiment (piC) are compared with those in the reanalyses from 1851 to 1896. FORTE2 reproduces the seasonality of precipitation in East China reasonably well, but slightly overestimates the averaged magnitude with about 1 mm/day in summer (Fig. 1a). However, the model underestimates the magnitude of South Asian Summer Monsoon precipitation by approximately 4 mm/day during June-September relative to the 20CR reanalysis. Dry biases in Indian summer precipitation of similar magnitudes are found in many CMIP5 and CMIP6 models (Sperber et al., 2013; Wilcox et al., 2020; Liu et al., 2024). Differences between reanalyses and observational datasets can also have similar magnitudes (Wilcox et al., 2020). Hence, we conclude that the FORTE2 representation of monsoon precipitation is suitable for our study. The model performs fairly well in the seasonality of temperature and the magnitudes in both

regions (Fig. 1b).

The simulated SLPs are generally lower than those in HadSLP in all four seasons, especially the Siberian High in winter, the western North Pacific Subtropical High (WPSH) and the Indian Low in summer (Fig. 1c-j). Compared to the reanalyses, the simulated Indian Low is overly strong, and its eastern fringe and the westerly from the Indian Ocean extend too far east into the western North Pacific, so does the Indian summer monsoon trough (Fig. 1g and h). This corresponds to the model dry bias over the Indian subcontinent (Fig. 1a and S3e-f). Meanwhile, the WPSH is too weak to expand sufficiently far west, corresponding to the very weak easterlies along the southern fringe of the WPSH, which leads to relatively less rainfall over the Philippines (Fig. S3e-f) and underestimates the effects of the WPSH on the East Asian summer monsoon (Fig. 1g-h). Despite these deficiencies, the model captures the essential features of lower tropospheric circulation, precipitation and temperature over Asia, which is consistent with the results of Stjern et al. (2024).

3.2 Temperature and Precipitation responses

Figure 2 shows spatial patterns of Ts responses to increased Asian BC aerosols in four seasons. First, there is a substantial land cooling over the perturbed regions in all four seasons, but with distinct seasonal differences in distributions and values. Under BC_CHI, a cooling is observed in most of China in winter and spring (Fig. 2a-b), with the area-averaged values of -0.9 ± 1.2 K (mean value \pm 1 standard deviation) and -1.1 ± 0.9 K, respectively (Fig. 3a). The large standard deviations indicate the large spread of distributions of responses (Fig. S4). There is a slight warming of sea surface temperatures near China in spring. In summer and autumn, a cooling is seen mainly in the region to the north of the Yangtze River valley, especially in North China, while there is a weak warming to the south (Fig. 2c-d). The area-averaged values are therefore relatively smaller than those in winter and spring, with values of approximately -0.7 ± 0.7 K for summer and autumn (Fig. 3a).

Under BC_IND, the strongest cooling occurs in the whole India in spring with the area-averaged value of -1.4 ± 1.4 K, but with a weak warming in the tropical Indian

Ocean (Fig. 2f and 3b). The significant cooling is concentrated in northern India in the other three seasons, with the area-averaged Ts decreased by 0.9 ± 1.3 K for winter and autumn, and 0.6 ± 1.1 K for summer (Fig. 2e, g, h and 3b). The ocean surrounding the Indian subcontinent shows a smaller cooling in the three seasons.

Secondly, the BC perturbations not only cause the local responses, but also non-local responses through atmospheric circulations. The increased BC over East China leads to a dipolar pattern in India with a warming to the north and a cooling to the south in summer and autumn, and a significant warming in Central Asia in summer and Southeast Asia in autumn (Fig. 2c-d). BC emissions over India can induce a cooling in Southeast Asia in all seasons, with the strongest responses occurring in summer (the averaged value of about 1.15 K). Meanwhile, there is a significant cooling in central and southern China in summer and autumn, with temperature decreases of 0.3 ± 0.7 K and 0.2 ± 0.7 K, respectively (Fig. 2g-h and 3a). These added impacts lead to a stronger East Asian cooling response under BC_CHI+IND than under BC_CHI in summer and autumn (Fig. 2k-l and 3a). Moreover, comparison between the combined regional responses and the sum of individual regional responses shows nearly insignificant differences, suggesting that the impact of Asian BC aerosol on the Asian Ts is regionally linear in all four seasons (Fig. S5).

In contrast to Ts responses, the responses in air temperature (Ta) at 850 hPa show a significant warming over much of the perturbed regions (Fig. 3c-d and 4). A cooling occurs over a few perturbed regions, such as central China under BC_CHI and BC_CHI+IND in winter (Fig. 4a, i). The vertical distribution of the temperature response is characterized by cooling at the surface and warming in the lower troposphere. This is a result of atmospheric absorption of solar shortwave radiation (SW) by BC aerosols, and is consistent with many previous studies (e.g., Li et al., 2016). Outside the perturbed regions, the Ta responses are in line with the Ts response, for example a cooling over China and Southeast Asia under BC_IND in summer and autumn (Fig. 3c and 4g, h).

Increased BC over East China primarily induces robust drying over most of China in all four seasons (Fig. 3e and 5a-d). Specifically, the spatial distribution in summer

shows a substantial decrease over southern China (up to 40%), a relatively weaker decrease over north China and a weak increase over northwest China, with the area-averaged precipitation decreased by 0.5 ± 0.5 mm/day (Fig. 3e, 5c and S6c). In spring and autumn, the decreased precipitation is mainly located in south and northeast China by up to about 40% (Fig. 5b and d). Although the absolute change is the weakest in winter (-0.2 ± 0.3 mm/day), the relative change in central China decreases by up to about 60% (Fig. 3e, 5a and S6a). Under BC_IND, the response over the Indian subcontinent is only statistically significant in summer, with a decrease of 0.5 ± 1.1 mm/day ($\sim 21\%$) (Fig. 3f and 5g).

Additionally, under BC_CHI there is increased rainfall over India in summer and autumn, which can counteract the local decrease due to the Indian BC forcing (Fig. 3f and 5c-d). Hence, when considering the simultaneous BC forcing in the two regions (BC_CHI+IND) in summer and autumn, there is no significant change in the regional mean, showing a dipolar pattern with more rainfall over northern India and less rainfall over southern India (Fig. 3f and 5k-l). On the other hand, BC_IND can induce a significant precipitation increase over China and Southeast Asia in spring and summer (Fig. 5f-g), partially offsetting the decrease in response to BC_CHI over China. Hence, the responses under BC_CHI+IND are weaker for China than those under BC_CHI (Fig. 3e). For regional linearity, the responses are almost linear (Fig. S7). Only a few regions exhibit nonlinear responses, such as a decrease over south Thailand in winter and an increase over northeast India in spring and summer. The above analysis regarding the summer part has been presented in Stjern et al. (2024), but is included here as a precursor to the detailed mechanistic analysis that follows.

3.3 Energy balance response

The following analysis mainly focuses on summer for clarity; the results for the other three seasons are in the supplement (Figures S9-S12, S14-S18). The spatial patterns of net TOA and surface energy responses to regional BC aerosols in summer are illustrated in figure 6. As expected, there are increases in net downward TOA shortwave (SW), with area mean responses of $7.3 \sim 9.6$ W/m² associated with decreases

in convective clouds over the perturbed regions (Fig. 6a-c and S8j-l). Decreases in net surface downward SW can be seen with area mean responses of $-22.6\sim-27.8\text{ W/m}^2$ due to SW absorption by BC aerosols (Fig. 6d-f). Significant increases in low and middle clouds also contribute to the reduced surface SW (Fig. S8d-i). Hence, there is warming in the troposphere while cooling at surface in these perturbed regions. The enhanced net surface upward longwave (LW) has a small contribution to the local surface cooling with area mean responses from -3.2 to -5.8 W/m^2 (Fig. 6g-i), which is related to the decreased convective clouds (Fig. S8j-l). On the contrary, the positive changes in downward sensible heat (SH) ($8.1\sim9.8\text{ W/m}^2$) and latent heat (LH) ($9.5\sim12.9\text{ W/m}^2$) cause a warming effect partly offsetting the cooling in the perturbation regions (Fig. 6j-o). The reduced SH is caused by the weakened vertical temperature differences between the surface and lower atmosphere. The decrease in upward LH is associated with upper-level heating through atmospheric stabilization that suppresses moisture transport, and reduced soil moisture availability due to decreased rainfall. Outside the perturbation regions, the negative changes in SW, LW and LH are responsible for the cooling in Southeast Asia and south China induced by the increased BC in India (Fig. 6e, h, n). Similar results can be seen in other three seasons (Table S2).

Figure 7 shows area-averaged atmospheric column energy budget terms (see Eq. 1) over East China and India in summer. For the drying in East China/India under BC_CHI/BC_IND, the substantial reductions of the diabatic cooling (δQ) are the prime driver of the decreases in the energy of precipitation ($L_c\delta P$), while the increases in the DSE flux divergence (δH) offset the effect of δQ to a large extent.

The enhanced precipitation in China under BC_IND, and in India under BC_CHI, is the result of increased δH (blue and green bars in Fig. 7 are almost identical), with negligible contribution from δQ . Hence, the local precipitation response to local BC increases is largely driven by δQ , while the remote precipitation response is largely driven by δH . Consequently, it can be found that the larger changes in δH lead to the smaller responses in $L_c\delta P$ over China and India under BC_CHI+IND, relative to the changes under BC_CHI and BC_IND. It should be mentioned that the relatively large uncertainties (error bars in Fig. 7) of $L_c\delta P$ mainly depend on δH . The other three

seasons show the similar results (Fig. S9).

Spatially, δQ shows a significant decrease throughout the entire perturbed regions in the three simulations, with large decreases located over North China and northern India (Fig. 8d-f). Under BC_CHI, δH exhibits a dipolar pattern with positive changes in north of the Yangtze River and negative in south (Fig. 8g). Hence, δH and δQ cancel each other out in North and Northeast China, while combine with each other in south of the Yangtze River. As a result, there is the strongest precipitation decrease in south China, and a relatively weaker decrease in north China (Fig. 8a). Under BC_IND, significant positive δH can be found along the southern edge of Himalayas and the southern tip of the Indian subcontinent, and weak and nonsignificant negative changes in central India (Fig. 8h). δH can therefore offset the negative changes in δQ in north and south India. The substantial $L_c\delta P$ reduction in central India is mainly driven by δQ (Fig. 8b).

In addition, δH is the dominating factor for $L_c\delta P$ beyond the perturbation regions, for example positive changes in northeast India under BC_CHI and from Southeast Asia to the tropical western Pacific and central China under BC_IND (Fig. 8g-h). Under BC_CHI+IND, the extent and magnitude of δH are larger than those in the simulations of individual regions (Fig. 8i), which indicates greater balance between δH and δQ , corresponding to relatively weaker precipitation over East China and India (Fig. 7 and 8c). Relative to summer, δQ and δH have negative and positive changes, respectively, throughout the perturbation regions in the other three seasons (Fig. S10-12). In winter and spring, there is a marked seesaw pattern of δH between Asia and the tropical Indian Ocean and maritime continent under BC_CHI+IND, reducing precipitation in the latter regions (Fig. S10c, i and S11c, i). Overall, the combined effect of δH and δQ shape the spatial pattern of precipitation responses to the regional BC.

The reductions in δQ (see Eq. 2) are dominated by the strong atmospheric heating due to SW absorption by BC aerosols ($-\delta SWA$), and also contributed by the small decreases in the atmospheric longwave cooling (δLWC) (Fig. S13a-f). The sensible heat flux from the surface ($-\delta SH$) slightly increases δQ (Fig. S13g-i).

3.4 Dynamic processes responsible for responses

Due to storage constraints, 3D atmospheric output from FORTE2 was archived on three pressure levels, 250 hPa, 500 hPa, and 850hPa, to capture key aspects of the tropospheric circulation response. While this precludes quantitative analysis of the component terms of H_m and H_{trans} , it is sufficient to identify the main contributor to H_m . We now examine the four terms of δH_m (see Eq. 3), including the dynamic components with changes in vertical and horizontal atmospheric circulations (δH_{Dyn_v} and δH_{Dyn_h}), and thermodynamic components with changes in vertical and horizontal DSE gradients (δH_{Thermo_v} and δH_{Thermo_h}). Figure 9 displays spatial patterns of the four components in summer in the three simulations. In general, the δH_{Dyn_v} highly resembles the δH in all simulations, and the magnitudes in δH_{Dyn_v} are far greater than those in the other three terms, suggesting that dynamic effect of vertical circulation is the primary contributor to δH (Fig. 9a-c). δH_{Thermo_v} and δH_{Dyn_h} show minimal anomalies in all regions for all experiments. Larger anomalies are seen in δH_{Thermo_h} , where negative anomalies offset some of the influence of δH_{Dyn_v} over the Indo-China peninsula in the BC_IND and BC_CHI+IND experiments. However, these anomalies are insufficient to influence the sign of δH , which is still primarily driven by δH_{Dyn_v} in this region. In the other seasons, δH_{Dyn_v} remains the most important factor (Fig. S14-16), although it is more strongly offset by δH_{Dyn_h} and δH_{Thermo_h} in winter. The effects of horizontal circulation are relatively weak in spring and autumn.

Based on the above analysis, we conclude that vertical movement is the primary contributor to δH_m . As expected, the spatial patterns of responses in vertical velocity (Ω) at 500 hPa correspond well to those in δH_{Dyn_v} (Fig. 10a-c). Anomalous ascent corresponds to the increase in δH_{Dyn_v} , leading to more precipitation, which offsets the precipitation reduction driven by decreased δQ . While anomalous descent amplifies precipitation suppression caused by the reduced δQ .

Why does the vertical velocity exhibit such changes? It seems to be related to the tropospheric temperature responses, reflected by a good corresponding relationship between the Omega and Ta responses at 500 hPa (Fig. 10a-f). The warm anomalies favor a divergence in the middle troposphere, which in turn are associated with anomalous ascent. The cold anomalies are associated with a convergence and descending motion. The above-mentioned relationship also exists in the other seasons, and it is more pronounced at 850 hPa (Fig. 4 and S17).

From the transects of zonal mean diabatic heating over the perturbation regions, changes to tropospheric heating can be seen more clearly (Fig. 11). Under BC_CHI, the responses in diabatic heating show a meridional dipolar structure through the whole troposphere over East China, with a cooling over the region to south of 32°N (the Yangtze River basin), and a warming to north (Fig. 11a). The dipolar pattern corresponds well to the meridional distributions of precipitation, vertical velocity and Ta at 500 hPa. The cooling center located at the middle troposphere is due to the reduced latent heat release caused by the substantial decrease in precipitation over south China. The heating center at the lower troposphere in the north mainly results from SW absorption by increased BC aerosol. The difference between south China and north China is associated with the larger AOD perturbation imposed north of the Yangtze basin in SyRAP-FORTE2 (Fig. S1). In BC_CHI+IND, there is a similar dipolar pattern, except for a warming at the lower troposphere around south of 30°N (Fig. 11b). The warming is related to the increased precipitation over south China because of the BC aerosols over India.

For India in BC_IND, there is also a cooling center associated with the reduced precipitation in the middle troposphere (Fig. 11c), corresponding to a cold anomaly and descending motion at 500 hPa (Fig. 10b, e). In the lower troposphere, a warming can be seen at south of the Qinghai-Tibet Plateau. Compared with BC_IND, the cold anomaly is weaker, but the warm anomalies are strengthened under BC_CHI+IND (Fig. 11d). Hence, a significant ascending motion can be found in northeast India resulted from the effect of increased BC over East Asia (Fig. 10c), which is consistent with that in Herbert et al. (2022). In the other three seasons, however, unlike in summer, there is

no cooling center in the middle troposphere, and the heating centers are situated at the lower troposphere (Fig. S18). Overall, the diabatic heating induced by the increased BC aerosols at the lower troposphere leads to an ascending motion explaining the increased δH over the perturbation regions.

Considering that the dynamic and thermodynamic effects of horizontal atmospheric circulations have some contributions to δH , we look at the changes in lower tropospheric horizontal circulation in response to changes of regional BC aerosols (Fig. 10g-i). Under BC_CHI, the cyclone anomaly over East China leads to anomalous easterly wind over North China with cutting off the moisture supply from south (Fig. 10g). Under BC_IND, the westerly anomalies associated with the cyclonic circulation over India favor to strength the Indian summer monsoon, which corresponds to the increase in δH_{Dyn_h} (Fig. 10h). The responses in the circulations to both regions at once can be seen as the sum of responses to the two separate regions (Fig. 10i). Additionally, there is a cyclonic circulation over East China and an anticyclonic circulation over central China in winter under BC_CHI (Fig. S19), leading to anomalous northerly wind across central China and then suppress precipitation over there, which is in agreement with the decrease in δH_{Dyn_h} (Fig. S14g). The changes in horizontal circulations are related to the changes in T_a and ω in the lower troposphere (Fig. 4 and S17).

4 Energy budget analysis in other coupled models

To evaluate the precipitation response and the mechanisms in FORTE2, we compare the results of energy budget analysis (see Eq. 1) in the PDRMIP simulations forced by 10 times the present-day Asian BC concentrations/emissions in five CMIP-class models to those in the SyRAP-FORTE2 BC_CHI+IND experiment. Spatial patterns of summer energy budgets in the PDRMIP and FORTE2 models are illustrated in Figure 12. There are significant decreases in δQ over most of Asia in all of the PDRMIP models, which is generally consistent with the results under BC_CHI+IND (Fig. 12g-l). Three models (CESM1-CAM5, GISS-E2-R and NorESM1) have similar

distributions of δQ to BC_CHI+IND, showing a maximum center in North China and northern India. δH increases significantly in India and most of East China in these models (Fig. 12m, n, q), again roughly resembling the changes of BC_CHI+IND (Fig. 12r), while the other two models show a significant increase in northern India and North China with weaker magnitudes (Fig. 12o-p). The PDRMIP multi-model mean changes in δH [figure 7 in Liu et al. (2018)] are also similar to the changes in BC_CHI+IND. In addition, GISS-E2-R and MIROC show evident decreases in δH and precipitation in Southeast Asia, while the other three models show no significant changes. This is contrary to the significant increases seen in FORTE2. There are large differences in the total $L_c\delta P$ responses across these models (Fig. 12a-f). However, some precipitation changes are consistent in most of the models, such as decreases over South China and increases over North China and northern India.

Figure 13 shows the regional means of each energy budget term over East China and India in summer under the PDRMIP and FORTE2 models. There is a weak and insignificant reduction in $L_c\delta P$ from -0.6 (HadGEM3) to -7.2 W/m² (NorESM1) for East China, which is comparable to the value of -3.8 W/m² under BC_CHI+IND (Fig. 13a). Hence, the increased BC perturbations over Asia lead to slight decreases in precipitation over East China in all of the models. The regional means range from -1.2 (MIROC) to 13.7 W/m² (NorESM1) for India (Fig. 13b). Except for MIROC, $L_c\delta P$ in the other models have stronger increases than that under BC_CHI+IND, about 0.6 W/m², which may be related to the larger drying bias of Indian summer precipitation in FORTE2, or the much larger BC perturbation in PDRMIP.

The effect of δQ decreases $L_c\delta P$ with a large range from -4.7 (HadGEM3) to -29.8 W/m² (GISS-E2-R) for East China, while δH has an opposite effect from 2.1 (MIROC) to 24.4 W/m² (GISS-E2-R) (Fig. 13a). Similarly, δQ changes from -5.7 (HadGEM3) to -25.8 W/m² (GISS-E2-R) for India, and δH from 4.9 (MIROC) to 36.5 W/m² (GISS-E2-R) (Fig. 13b). The magnitudes in δQ and δH under the PDRMIP models are much smaller than those in FORTE2 in both regions, except for GISS-E2-R. The negative effect of δQ and the positive effect of δH can also be seen in the PDRMIP multimodel mean for the whole Asian region (Liu et al., 2018). There are substantial differences in

the magnitudes and spatial patterns of their responses, which are to be expected from their large range of aerosol radiative forcing and climatological precipitation. However, these precipitation responses among these models are overall consistent qualitatively, indicating that thermodynamic processes dominantly decrease precipitation, while dynamic processes increase precipitation and partially offset the effects of δQ .

5 Conclusion and Discussion

In this study, we have investigated the Asian climatic responses to adding BC aerosols to the separate regions (East China and India), and both regions at once, and examined the associated physical processes, with the SyRAP simulations based on the reduced-complexity climate model FORTE2. Our main findings are as follows.

i. BC increases over East Asia or South Asia lead to a local strong surface cooling and lower tropospheric air temperature warming in all four seasons, with seasonal differences in magnitude and spatial distribution. The responses in temperature are dominated by the substantial decreases in surface SW radiation due to SW absorption by BC aerosols. BC over East Asia causes significant drying in south and northeast China in spring, summer and autumn. In winter, there is a significant reduction in central China. BC over South Asia induces a substantial decrease in rainfall in India in summer. Also, South Asian BC induces significant temperature decreases and precipitation increases in Southeast Asia during summer and autumn.

ii. Responses in temperature and precipitation to Asian BC forcing are mostly linear regionally in all four seasons. There are relatively smaller decreases in precipitation responses to adding BC over both regions simultaneously, compared to the local reductions in precipitation responses to BC increases over East Asia and South Asia separately. This is because BC over East Asia (BC over India) increases precipitation in northeastern India, while BC over South Asia increases precipitation over southern and central China.

iii. Using an energy budget analysis, we find that reductions in the energy of local precipitation ($L_c\delta P$) over the perturbation regions result from decreases in net atmospheric diabatic cooling (δQ). The increases in the dry static energy (DSE) flux

divergence (δH) play a role in offsetting the effects of δQ to a large extent. Consequently, the responses in precipitation to Asian BC can be considered as the result of interactions between thermodynamic and dynamic processes. For δQ , the reductions are mainly due to the strong atmospheric heating ($-\delta SWA$). For δH , the increases depend mainly on the positive changes in the dynamic processes associated with vertical atmospheric circulations (δH_{Dyn_v}). We find that δH_{Dyn_v} patterns correspond well to vertical velocity change patterns at the middle and lower troposphere. Anomalous ascent is primarily triggered by the warming in the middle and lower troposphere over north China in summer and in most of Asia in the other seasons. However, there is anomalous descent in southern China and central India in summer, which is a result of cool anomalies in the middle troposphere due to the reduced latent heat release caused by the substantial decrease in precipitation. The difference in diabatic heating at the middle and lower troposphere is related to the difference in spatial distributions of AOD in the different seasons.

It is well known that the EASM and SASM underwent weakening trends during the second half of the 20th century (Wang et al., 2001; Bollasina et al., 2011). Although the variations of ASM have been attributed to many factors including internal variability and external forcing, the strong increases in BC emissions from East and South Asia (Lund et al., 2019) could play a role in weakening the ASM over the past decades according to this study. The increased BC could also alleviate the enhanced precipitation over south China due to GHG increase since the mid-1990s (Tian et al., 2018). Since the early 2010s, anthropogenic aerosols (including BC and sulfate) have been decreasing in East China, while they have continued to rise in India; these are trends which are expected to continue over the coming decades (Lund et al., 2019; Samset et al., 2019). Hence, there is a new dipole pattern characterized by decreasing aerosols over East China and increasing aerosols over India. Given that responses to Asian BC forcing are linear regionally in the SyRAP-FORTE2 simulations, the impacts of the dipole pattern on the Asian climate can be roughly estimated by the sum of responses to BC over China multiplied by -1 and responses to BC over India. The result

shows that there are warm anomalies in north China and cold anomalies in south China, southeast Asia and most of India, and positive precipitation anomalies over most of China (especially south China) and southeast Asia, and negative anomalies over India (Fig. S20). It is overall consistent with the result in Xiang et al. (2023), although their result involves the combined effect of BC and sulfate.

Comparative analysis with the CGCMs/ESMs results from PDRMIP has elucidated the key physical mechanisms of Asian climate responses to regional BC perturbations. The thermodynamic process dominates the precipitation reduction, while the dynamic process provides partial compensation. The SyRAP-FORTE2 experiment series allows systematic comparison of impacts of different Asian subregions, aerosol species, and climate backgrounds within a consistent modeling framework. Notably, FORTE2 includes a parameterization of ACI, enabling direct comparison of the relative contributions of ARI and ACI. These related works will be conducted in next step, and may provide new insights into regional aerosol impacts.

Large differences in the magnitude and spatial pattern of precipitation responses to BC exist across all the models. These discrepancies may partly be due to the much larger BC perturbation in PDRMIP, and partly be due to model-specific differences. The FORTE2 simulation only accounts for ARI effects, incorporating the semi-direct effect of BC, while PDRMIP models exhibit varying treatments of indirect effects. The models with all aerosol indirect effects (particularly CESM1-CAM5 and NorESM1) increase precipitation over India, contrasting with the reduced precipitation in FORTE2. Additionally, despite the much weaker BC forcing in FORTE2, it produces larger thermodynamic (δQ) and dynamic (δH) responses than most PDRMIP models (except for GISS-E2-R). This may arise from the absence of wet deposition feedbacks in FORTE2 (Stjern et al., 2024). Further work to understand the mechanisms behind model differences in the response to BC would help to reduce uncertainties and improve the confidence in future Asian climate change projections.

Acknowledgements. This work is supported by the Second Tibetan Plateau Scientific Expedition and Research Program (2019QZKK010203). Some of the research

presented in this paper was carried out on the High Performance Computing Cluster supported by the Research and Specialist Computing Support service at the University of East Anglia. We acknowledge the Center for Advanced Study in Oslo, Norway that funded and hosted our HETCLIF centre during the academic year of 2023/24. F. L. is supported by the Scientific Research of Chengdu University of Information Technology (Grant No. KYTZ202210). B. H. S., C. W. S., L. J. W., M. J. and R. J. A were supported by the Research Council of Norway [Grant 324182 (CA3THY)]. The authors acknowledge the editor, Yuan Wang, and the two anonymous reviewers for their valuable comments to improve the paper.

Data availability. The NOAA-CIRES-DOE 20th Century Reanalysis V3 (20CR) datasets are obtained from https://psl.noaa.gov/data/gridded/data.20thC_ReanV3.html. The HadSLP2r is provided by the UK Met Office Hadley Centre and can be downloaded from at <http://www.metoffice.gov.uk/hadobs/hadslp2/>. The PDRMIP data can be accessed through the World Data Center for Climate (WDCC) data server at https://doi.org/10.26050/WDCC/PDRMIP_2012-2021. Data of the SyRAP-FORTE2 experiments reported in this paper are available without restriction on reasonable request from Camilla W. Stjern at CICERO Center for International Climate Research.

Author contribution. F. L. and B. H. S. designed the study. C. W. S., L. J. W., M. J. ran the model simulations. F. L. carried out the analysis and visualized the results. All authors discussed the results and edited the paper.

Competing interests. L. J. W. is a member of the editorial board of *Atmospheric Chemistry and Physics*.

References

- Allan, R. and Ansell, T.: A new globally-complete monthly historical gridded mean sea level pressure dataset (HadSLP2): 1850-2004, *J. Climate*, 19, 5816-5842, <https://doi.org/10.1175/JCLI3937.1>, 2006.
- Betts, A. K. and Miller, M. J.: The Betts-Miller scheme, in: *The Representation of*

626 Cumulus Convection in Numerical Models of the Atmosphere, Chapter 9, edited
 627 by: Emanuel, K. A. and Raymond, D. J., Amer. Meteor. Soc., Meteor. Mon., 24,
 628 107-121, 1993.

629 Blaker, A. T., Joshi, M., Sinha, B., Stevens, D. P., Smith, R. S., and Hirschi, J. J.-M.:
 630 FORTE 2.0: a fast, parallel and flexible coupled climate model, Geosci. Model
 631 Dev., 14, 275-293, 10.5194/gmd-14-275-2021, 2021.

632 Bollasina, M. A., Ming, Y. and Ramaswamy, V.: Anthropogenic aerosols and the
 633 weakening of the South Asian summer monsoon, Science, 334, 502-505,
 634 <https://doi.org/10.1126/science.1204994>, 2011.

635 Bond, T. C., Doherty, S. J., Fahey, D. W., Forster, P., Berntsen, T., DeAngelo, B.,
 636 Flanner, M., Ghan, S., Kacher, B., Koch, D., Kinne, S., Kondo, Y., Quinn, P. K.,
 637 Sarofim, M. C., Schultz, M. G., Schulz, M., Venkataraman, C., Zhang, H., Zhang,
 638 S., Bellouin, N., Guttikunda, S. K., Hopke, P. K., Jacobson, M. Z., Kaiser, J. W.,
 639 Klimont, Z., Lohmann, U., Schwarz, J. P., Shindell, D., Storelvmo, T., Warren, S.
 640 G., and Zender, C. S.: Bounding the role of black carbon in the climate system: A
 641 scientific assessment, J. Geophys. Res.-Atmos., 118, 5380-552, 2013.

642 Chen, H., Zhuang, B., Liu, J., Li, S., Wang, T., Xie, X., Xie, M., Li, M. and Zhao, M.:
 643 Regional Climate Responses in East Asia to the Black Carbon Aerosol Direct
 644 Effects from India and China in Summer, J. Climate, 33, 9783-9800,
 645 <https://doi.org/10.1175/JCLI-D-19-7620706.1>, 2020.

646 Compo, G. P., Whitaker, S., Sardeshmukh, J., Matsui, N., Allan, R. J., Yin, X., Gleason,
 647 B. E., Vose, R. S., Rutledge, G., Bessemoulin, P., Bronnimann, S., Brunet,
 648 M., Crouthamel, R. I., Grant, A. N., Groisman, P. Y., Jones, P. D., Kruk, M.
 649 C., Kruger, A. C., Marshall, G. J., Maugeri, M., Mok, H. Y., Nordli, ., Ross, T.
 650 F., Trigo, R. M., Wang, X. L., Woodruff, S. D. and Worley, S. J.: The Twentieth
 651 Century Reanalysis Project, Q. J. Roy. Meteor. Soc., 137, 1-28, 2011.

652 Deng, J., Xu, H., Ma, H., Jiang Z.: Numerical study of the effect of anthropogenic
 653 aerosols on spring persistent rain over eastern China, J. Meteorol. Res., 28, 341-
 654 353, 2014.

655 Dong, B., Wilcox, L. J., Highwood, E. J., and Sutton, R. T.: Impacts of recent decadal

656 changes in Asian aerosols on the East Asian summer monsoon: roles of aerosol–
 657 radiation and aerosol–cloud interactions, *Clim. Dyn.*, 53, 3235–3256,
 658 <https://doi.org/10.1007/s00382-019-04698-0>, 2019.

659 Granier, C., Bessagnet, B., Bond, T., D’Angiola, A., Denier van der Gon, H., Frost, G.
 660 J., Heil, A., Kaiser, J. W., Kinne, S., Klimont, Z., Kloster, S., Lamargue, J. F.,
 661 Liousse, C., Masui, T., Meleux, F., Mieville, A., Ohara, T., Raut, J. C., Riahi, K.,
 662 Schultz, M. G., Smith, S. J., Thompson, A., Aardenne, J., van der Werf, G. R., and
 663 van Vuuren, D. P.: Evolution of anthropogenic and biomass burning emissions of
 664 air pollutants at global and regional scales during the 1980–2010 period, *Climatic*
 665 *Change*, 109, 163–190, <https://doi.org/10.1007/s10584-011-0154-1>, 2011.

666 Gu, Y., Liou, K. N., Xue, Y., Mechoso, C. R., Li, W. and Luo, Y.: Climatic effects of
 667 different aerosol types in China simulated by the UCLA general circulation model,
 668 *J. Geophys. Res.*, 111, D15201, doi:10.1029/2005JD006312, 2006.

669 Guo, L., Highwood, E. J., Shaffrey, L. C. and Turner, A. G.: The effect of regional
 670 changes in anthropogenic aerosols on rainfall of the East Asian Summer Monsoon,
 671 *Atmos. Chem. Phys.*, 13, 1521–1534, <https://doi.org/10.5194/acp-13-1521-2013>,
 672 2013.

673 Guo, L., Turner, A. and Highwood, E.: Impacts of 20th century aerosol emissions on
 674 the South Asian monsoon in the CMIP5 models, *Atmos. Chem. Phys.*, 15, 6367–
 675 6378, <https://doi.org/10.5194/acp-15-6367-2015>, 2015.

676 Herbert, R., Wilcox, L. J., Joshi, M., Highwood, E. and Frame, D.: Nonlinear response
 677 of Asian summer monsoon precipitation to emission reductions in South and East
 678 Asia, *Environ. Res. Lett.*, 17, 014005, [10.1088/1748-9326/ac3b19](https://doi.org/10.1088/1748-9326/ac3b19), 2022.

679 Hu, N. and Liu, X.: Modeling study of the effect of anthropogenic aerosols on late
 680 spring drought in South China, *Acta Meteorol. Sin.*, 27, 701–715,
 681 doi:10.1007/s13351-013-0506-z, 2014.

682 Inness, A., Ades, M., Agustí-Panareda, A., Barré, J., Benedictow, A., Blechschmidt, A.-
 683 M., Dominguez, J. J., Engelen, R., Eskes, H., Flemming, J., Huijnen, V., Jones, L.,
 684 Kipling, Z., Massart, S., Parrington, M., Peuch, V.-H., Razinger, M., Remy, S.,

- Schulz, M., and Suttie, M.: The CAMS reanalysis of atmospheric composition, *Atmos. Chem. Phys.*, 19, 3515-3556, 10.5194/acp-19-3515-2019, 2019.
- IPCC, 2021: Climate Change 2021: The Physical Science Basis. Contribution of Working Group I to the Sixth Assessment Report of the Intergovernmental Panel on Climate Change [Masson-Delmotte, V., P. Zhai, A. Pirani, S.L. Connors, C. Péan, S. Berger, N. Caud, Y. Chen, L. Goldfarb, M.I. Gomis, M. Huang, K. Leitzell, E. Lonnoy, J.B.R. Matthews, T.K. Maycock, T. Waterfield, O. Yelekçi, R. Yu, and B. Zhou (eds.)]. Cambridge University Press, Cambridge, United Kingdom and New York, NY, USA, 2391 pp. doi:10.1017/9781009157896.
- Jiang, Y., Liu, X., Yang, X. Q. and Wang, M.: A numerical study of the effect of different aerosol types on East Asian summer clouds and precipitation, *Atmos. Environ.*, 70, 51-63, 2013.
- Jiang, Y., Yang, X. Q., Liu, X., Yang, D., Sun, X., Wang, M., Ding, A., Wang, T. and Fu, C.: Anthropogenic aerosol effects on East Asian winter monsoon: The role of black carbon-induced Tibetan Plateau warming, *J. Geophys. Res. Atmos.*, 122, 5883-5902, doi:10.1002/2016JD026237, 2017.
- Joshi, M., Stringer, M., van der Wiel, K., O'Callaghan, A. and Fueglistaler, S.: IGCM4: a fast, parallel and flexible intermediate climate model, *Geosci. Model Dev.*, 8, 1157-1167, 10.5194/gmd-8-1157-2015, 2015.
- Lau, K. M., Kim, M. K. and Kim, K. M.: Asian monsoon anomalies induced by aerosol direct forcing: the role of the Tibetan Plateau, *Clim. Dynam.*, 26, 855-664, 2006.
- Lau, K. M. and Kim, K. M.: Does aerosol strengthen or weaken the Asian monsoon? in *Mountains: Witnesses of Global Change*, edited by: Baudo, R., Tartari, G., and Vuillermoz, E., Elsevier, Amsterdam, the Netherlands, 2007.
- Li, J., Carlson, B. E., Yung, Y. L., Lv, D., Hansen, J., Penner, J., Liao, H., Ramaswamy, V., Kahn, R., Zhang, P., Dubovik, O., Ding, A., Lacis, A., Zhang, L. and Dong, Y.: Scattering and absorbing aerosols in the climate system, *Nat. Rev. Earth. Environ.*, 3, 363-379, <https://doi.org/10.1038/s43017-022-00296-7>, 2022.
- Li, Z., Lau, W. K., Ramanathan, V., Wu, G., Ding, Y., Manoj, M. G., Liu, J., Qian, Y., Li, J., Zhou, T., Fan, J., Rosenfeld, D., Ming, Y., Wang, Y., Huang, J., Wang, B.,

- Xu, X., Lee, S. S., Cribb, M., Zhang, F., Yang, X., Takemura, T., Wang, K., Xia, X., Yin, Y., Zhang, H., Guo, J., Zhai, P. M., Sugimoto, N., Babu, S. S., and Brasseur, G. P.: Aerosol and Monsoon Climate Interactions over Asia, *Rev. Geophys.*, 54, 866–929, <https://doi.org/10.1002/2015rg000500>, 2016.
- Liu, L., Shawki, D., Voulgarakis, A., Kasoar, M., Samset, B. H., Myhre, G., Forster, P. M., Hodnebrog, Ø, Sillmann, J., Aalbergstjø, S. G., Boucher, O., Faluvegi, G., Iversen, T., Kirkevåg, A., Lamarque, J., Olivié, D., Richardson, T., Shindell, D. and Takemura, T.: A PDRMIP Multimodel Study on the Impacts of Regional Aerosol Forcings on Global and Regional Precipitation, *J. Climate*, 31, 4429–4447, <https://doi.org/10.1175/JCLI-D-17-0439.1>, 2018.
- Liu, Z., Bollasina, M. and Wilcox, L.: Impact of Asian aerosols on the summer monsoon strongly modulated by regional precipitation biases, *EGUsphere* [preprint], <https://doi.org/10.5194/egusphere-2023-3136>, 2024.
- Lou, S., Yang, Y., Wang, H., Lu, J., Smith, S., Liu, F. and Rasch, P.: Black Carbon Increases Frequency of Extreme ENSO Events, *J. Climate*, 32, 8323–33, <https://doi.org/10.1175/JCLI-D-19-0549.1>, 2019.
- Lou, S., Yang, Y., Wang, H., Smith, S., Qian, Y. and Rasch, P.: Black carbon amplifies haze over the North China Plain by weakening the East Asian winter monsoon, *Geophys. Res. Lett.*, 46, 452–460, <https://doi.org/10.1029/2018GL080941>, 2019.
- Lund, M. T., Myhre, G. and Samset, B. H.: Anthropogenic aerosol forcing under the Shared Socioeconomic Pathways, *Atmos. Chem. Phys.*, 19, 13827–13839, <https://doi.org/10.5194/acp-19-13827-2019>, 2019.
- Mahmood, R. and Li, S.: Remote influence of South Asian black carbon aerosol on East Asian summer climate, *Int. J. Clim.*, 34, 36–48, <https://doi.org/10.1002/joc.3664>, 2014.
- Meehl, G. A., Arblaster, J. M. and Collins, W. D.: Effects of black carbon aerosols on the Indian monsoon, *J. Climate*, 21, 2869–2882, <https://doi.org/10.1175/2007JCLI1777.1>, 2008.
- Muller, C. J. and O’Gorman, P. A.: An energetic perspective on the regional response of precipitation to climate change. *Nat. Climate Change*, 1, 266–271,

745 <https://doi.org/10.1038/nclimate1169>, 2011.

746 Menon, S., Hansen, J., Nazarenko, L., Nazarenko, L. and Luo, Y.: Climate effects of
 747 black carbon aerosols in China and India, *Science*, 297, 2250-2253, 2002.

748 Myhre, G., Forster, P., Samset, B., Hodnebrog, Ø, Sillmann, J., Aalbergstjø, S. G.,
 749 Andrews, T., Boucher, O., Faluvegi, G. and Flächner, D.: PDRMIP: A precipitation
 750 driver and response model intercomparison project, protocol and preliminary
 751 results, *B. Am. Meteorol. Soc.*, 98, 1185-1198, [https://doi.org/10.1175/BAMSD-](https://doi.org/10.1175/BAMSD-16-0019.1)
 752 16-0019.1, 2017.

753 Persad, G. G., Paynter, D. J., Ming, Y. and Ramaswamy, V.: Competing Atmospheric
 754 and Surface-Driven Impacts of Absorbing Aerosols on the East Asian Summertime
 755 Climate, *J. Climate*, 30, 8929-49, <https://doi.org/10.1175/JCLI-D-16-0860.1>, 2017.

756 Ramanathan, V. and Carmichael, G.: Global and regional climate changes due to black
 757 carbon, *Nat. Geosci.*, 1, 221-227, <https://doi.org/10.1038/ngeo156>, 2008.

758 Recchia, L. G. and Lucarini, V.: Modelling the effect of aerosol and greenhouse gas
 759 forcing on the South Asian and East Asian monsoons with an intermediate-
 760 complexity climate model, *Earth Syst. Dynam.*, 14, 697-722, 10.5194/esd-14-697-
 761 2023, 2023.

762 Riahi, K., Rao, S., Krey, V., Cho, C., Chirkov, V., Fischer, G., Kindermann, G.,
 763 Nakicenovic, N., Rafaj, P.: Rcp 8.5—A scenario of comparatively high greenhouse
 764 gas emissions, *Climatic Change*, 109, 33-57, [https://doi.org/10.1007/s10584-011-](https://doi.org/10.1007/s10584-011-0149-y)
 765 [0149-y](https://doi.org/10.1007/s10584-011-0149-y), 2011.

766 Richardson, T. B., Forster, P. M., Andrews, T. and Parker, D.: Understanding the rapid
 767 precipitation response to CO₂ and aerosol forcing on a regional scale. *J. Climate*,
 768 29, 583-594, <https://doi.org/10.1175/JCLI-D-15-0174.1>, 2016.

769 Samset, B. H., Lund, M. T., Bollasina, M., Myhre, G. and Wilcox, L.: Emerging Asian
 770 aerosol patterns, *Nat. Geosci.*, 12, 582-584, [https://doi.org/10.1038/s41561-019-](https://doi.org/10.1038/s41561-019-0424-5)
 771 0424-5, 2019.

772 Sperber, K. R., Annamalai, H., Kang, I. S., Kitoh, A., Moise, A., Turner, A., Wang, B.
 773 and Zhou, T.: The Asian summer monsoon: an intercomparison of CMIP5 vs.

774 CMIP3 simulations of the late 20th century, *Clim. Dynam.*, 41, 2711-2744,
775 10.1007/s00382-012-1607-6, 2013.

776 Stier, P., van den Heever, S. C., Christensen, M. W., Gryspeerdt, E., Dagan, G., Saleeby,
777 S. M., Bollasina, M., Donner, L., Emanuel, K., Ekman, A. M. L., Feingold, G.,
778 Field, P., Forster, P. and Haywood, J.: Multifaceted Aerosol Effects on
779 Precipitation, *Nat. Geosci.*, 17, 719-732, [https://doi.org/10.1038/s41561-024-](https://doi.org/10.1038/s41561-024-01482-6)
780 [01482-6](https://doi.org/10.1038/s41561-024-01482-6), 2024.

781 Stjern, C. W., Samset, B. H., Myhre, G., Forster, P. M., Hodnebrog, Ø, Andrews, T.,
782 Boucher, O., Faluvegi, G., Iversen, T., Kassoar, M., Kharin, V., Kirkevåg, A.,
783 Lamarque, J.-F., Olivieri, D., Richardson, T., Shawki, D., Shindell, D., Smith, C.,
784 Takemura, T. and Voulgarakis, A.: Rapid adjustments cause weak surface
785 temperature response to increased black carbon concentrations, *J. Geophys. Res.-*
786 *Atmos.*, 122, 11462-1481, <https://doi.org/10.1002/2017JD027326>, 2017.

787 Stjern, C., Joshi, M., Wilcox, L., Gollo, A. and Samset, B.: Systematic Regional Aerosol
788 Perturbations (SyRAP) in Asia using the intermediate-resolution global climate
789 model FORTE2, *J. Adv. Mod. Earth System*, accepted, 2024.

790 Tian, F., Dong, B., Robson, J. and Sutton, R.: Forced decadal changes in the East Asian
791 summer monsoon: the roles of greenhouse gases and anthropogenic aerosols, *Clim.*
792 *Dynam.*, <https://doi.org/10.1007/s00382-018-4105-7>, 2018.

793 Wang, H.: The weakening of the Asian monsoon circulation after the end of 1970's, *Adv.*
794 *Atmo. Sci.*, 18, 376-386, <https://doi.org/10.1007/BF02919316>, 2001.

795 Wang, Z., Lin, L., Yang, M., Xu, Y. and Li, J.: Disentangling fast and slow responses of
796 the East Asian summer monsoon to reflecting and absorbing aerosol forcings,
797 *Atmos. Chem. Phys.*, 17, 11075-11088, [https://doi.org/10.5194/acp-17-11075-](https://doi.org/10.5194/acp-17-11075-2017)
798 2017, 2017.

799 Webb, D. J.: An ocean model code for array processor computers, *Comput. Geosci.*, 22,
800 569-578, 1996.

801 Westervelt, D. M., Conley, A. J., Fiore, A. M., Lamarque, J.-F., Shindell, D. T., Previdi,
802 M., Mascioli, N. R., Faluvegi, G., Correa, G., and Horowitz, L. W.: Connecting
803 regional aerosol emissions reductions to local and remote precipitation responses,

- Atmos. Chem. Phys., 18, 12461-12475, [https://doi.org/10.5194/acp-18-12461-](https://doi.org/10.5194/acp-18-12461-2018)
2018, 2018.
- Westervelt, D. M., You, Y., Li, X., Ting, M., Lee, D. and Ming, Y.: Relative importance of greenhouse gases, sulfate, organic carbon, and black carbon aerosol for South Asian monsoon rainfall changes, *Geophys. Res. Lett.*, 47, e2020GL088363, <https://doi.org/10.1029/2020GL088363>, 2020.
- Wilcox, L. J., Liu, Z., Samset, B. H., Hawkins, E., Lund, M. T., Nordling, K., Undorf, S., Bollasina, M., Ekman, A. M. L., Krishnan, S., Merikanto, J., and Turner, A. G.: Accelerated increases in global and Asian summer monsoon precipitation from future aerosol reductions, *Atmos. Chem. Phys.*, 20, 11955–11977, <https://doi.org/10.5194/acp-20-11955-2020>, 2020.
- Xiang, B., Xie, S. P., Kang, S. M., and Kramer, R.: An emerging Asian aerosol dipole pattern reshapes the Asian summer monsoon and exacerbates northern hemisphere warming, *npj Clim. Atmos. Sci.*, 6, 77, [https://doi.org/10.1038/s41612-023-](https://doi.org/10.1038/s41612-023-00400-8)
00400-8, 2023.
- Xie, X., Myhre, G., Liu, X., Li, X., Shi, Z., Wang, H., Kirkevåg, A., Lamarque, J. F., Shindell, D., Takemura, T., and Liu, Y.: Distinct responses of Asian summer monsoon to black carbon aerosols and greenhouse gases, *Atmos. Chem. Phys.*, 20, 11823-11839, <https://doi.org/10.5194/acp-20-11823-2020>, 2020.
- Yang, J., Kang, S., Chen, D., Zhao, L., Ji, Z., Duan, K., Deng, H., Tripathee, L., Du, W., Rai, M., Yan, F., Li, Y. and Gillies, R.: South Asian black carbon is threatening the water sustainability of the Asian Water Tower, *Nat. Commun.*, 13, 7360, <https://doi.org/10.1038/s41467-022-35128-1>, 2022.
- Zhang, H., Wang, Z., Guo, P., and Wang, Z.: A modeling study of the effects of direct radiative forcing due to carbonaceous aerosol on the climate in East Asia, *Adv. Atmos. Sci.*, 26, 57-66, <https://doi.org/10.1007/s00376-009-0057-5>, 2009.
- Zhong, W. Y. and Haigh, J. D.: Improved broad-band emissivity parameterization for water vapor cooling calculations, *J. Atmos. Sci.*, 52, 124-148, 1995.

833 **Table 1.** Summary of SyRAP-FORTE2 simulations used in the study

Experiment ^a	Name	Aerosol	Region	GHG	Years
Baseline	piC	No aerosol	--	Preindustrial climate conditions (280 ppmv)	200
Perturbation	BC_CHI	Added BC ^b	East China (95-133°E, 20-53°N)		
	BC_IND		India (65-95°E, 5-35°N)		
	BC_CHI+IND		both East China and India region		

834 a. only ARI effect is considered

835 b. CAMSRA monthly climatology of BC AOD for 2003-2021

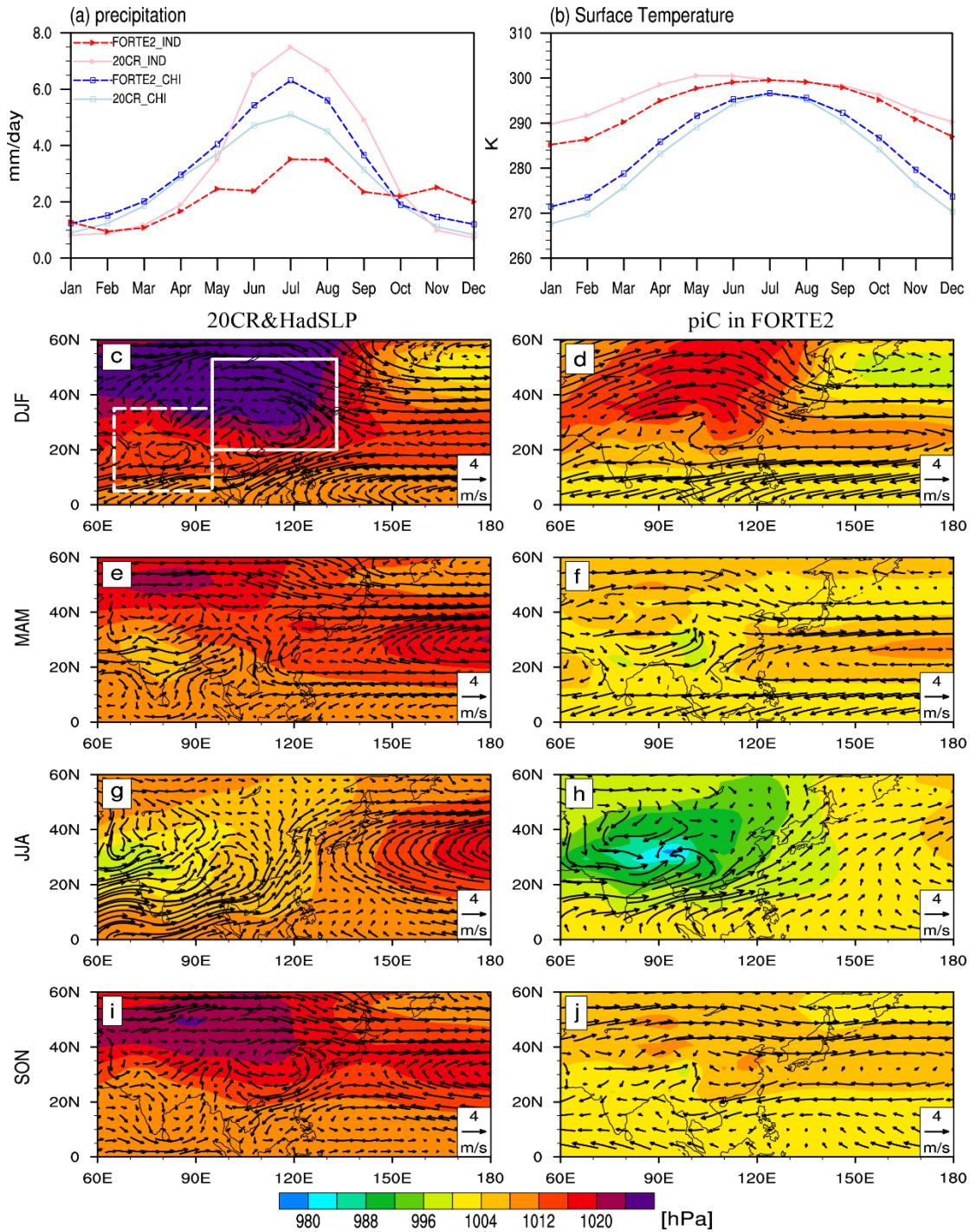


Figure 1. Seasonal evolutions of (a) the regional mean precipitation (unit: mm/day) of 20CR (solid lines) and the baseline simulation of FORTE2 (dashed lines) for East Asia (95°E-133°E, 20°N-53°N, the solid, white box in (c)) (light blue and blue lines), and India (65°E-95°E, 5°N-35°N, the dashed, white box in (c)) (pink and red lines). (b) same as (a), but for surface temperature (unit: K). Climate state of SLP (unit: hPa) and 850 hPa horizontal winds (unit: m/s) in (left) 20CR and HadSLP and (right) the baseline simulation of FORTE2 in four seasons (c-j).

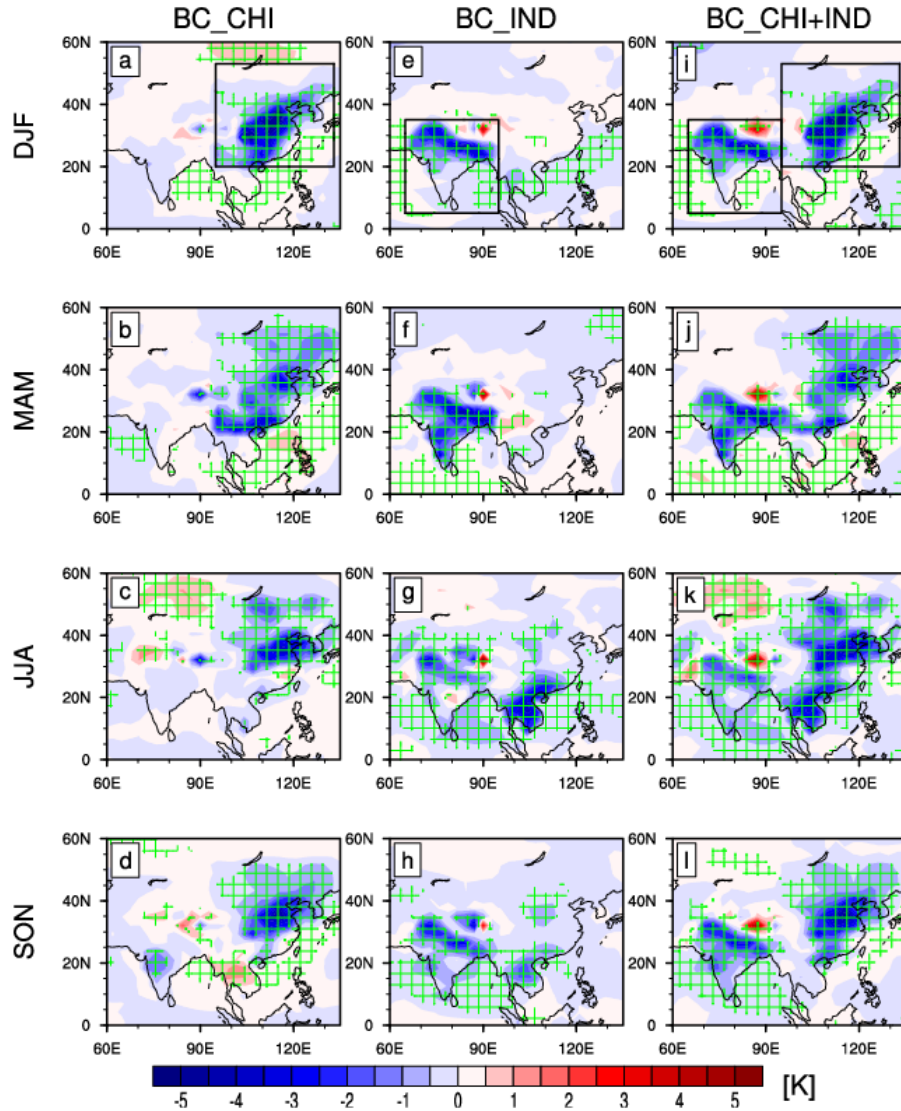


Figure 2. Spatial patterns of Ts responses in (a-d) BC_CHI, (e-h) BC_IND, and (i-l) BC_CHI+IND for four seasons. The green gridlines indicate the regions where the responses are statistically significant above 95% level based on a two-tailed Student's t-test. The black boxes in (a), (e) and (i) highlight the region where BC aerosols are perturbed. Unit: K

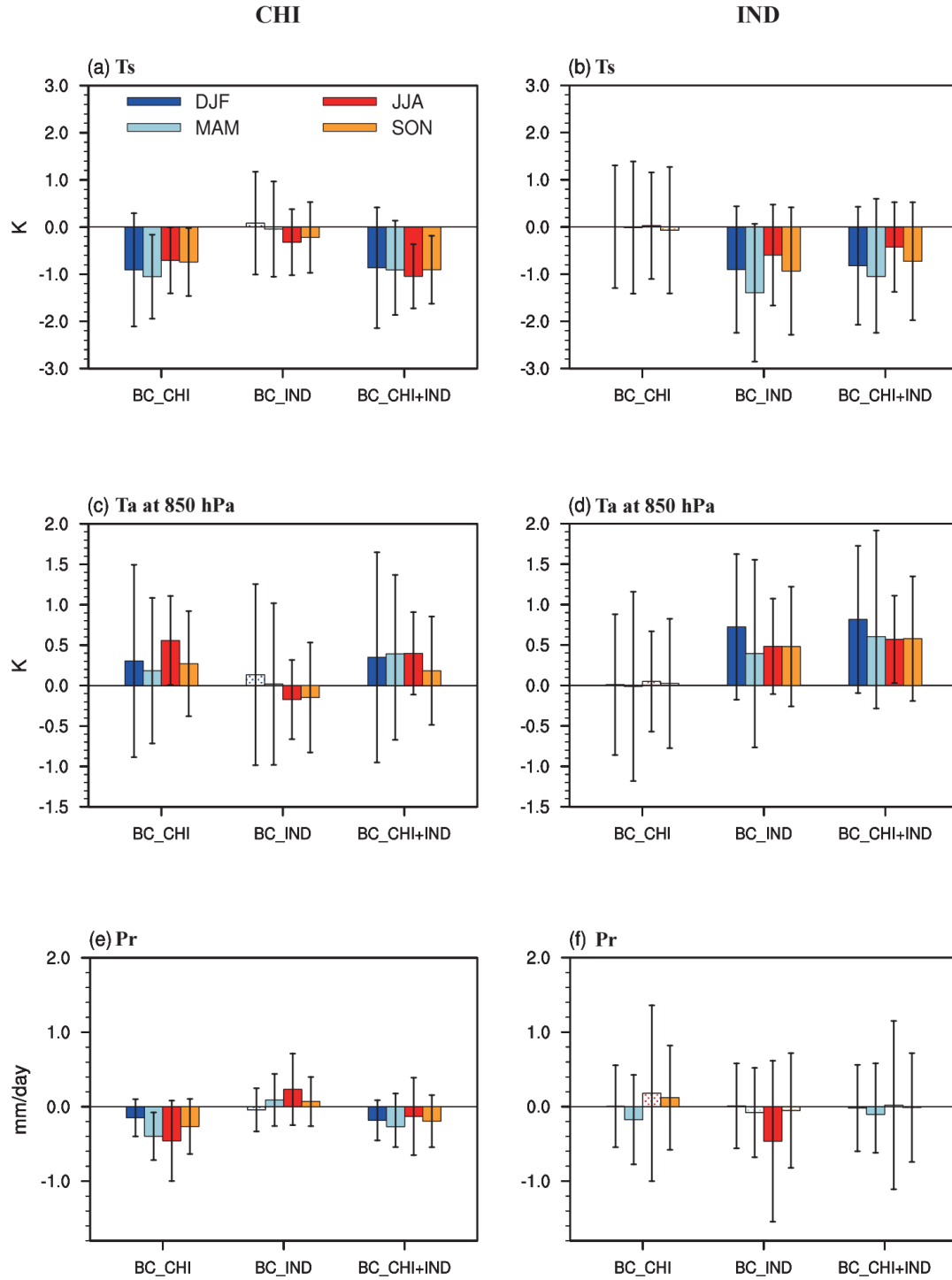


Figure 3. Area-averaged land responses of (a-b) Ts, (c-d) Ta at 850 hPa, and (e-f) precipitation over East China (CHI: 95°E-133°E, 20°N-53°N) and India (IND: 65°E-95°E, 5°N-35°N) for four seasons (DJF: blue bars, MAM: light blue bars, JJA: red bars, and SON: yellow bars). Solid bars indicate the responses are statistically significant above 95% level based on a two-tailed Student's t-test. Error bars represent ± 1 standard deviations of the response.

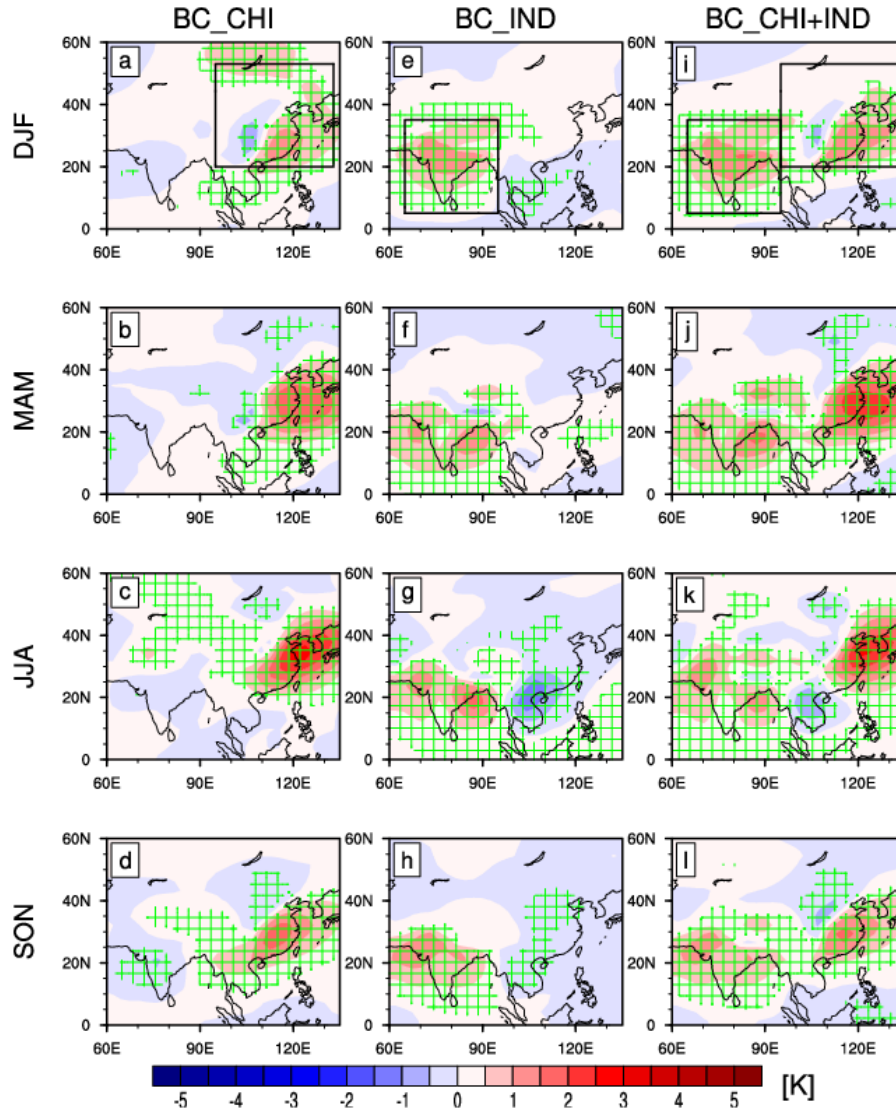


Figure 4. Spatial patterns of Ta responses at 850 hPa in (a-d) BC_CHI, (e-h) BC_IND, and (i-l) BC_CHI+IND for four seasons. The green gridlines indicate the regions where the responses are statistically significant above 95% level based on a two-tailed Student's t-test. The black boxes in (a), (e) and (i) highlight the region where BC aerosols are perturbed. Unit: K

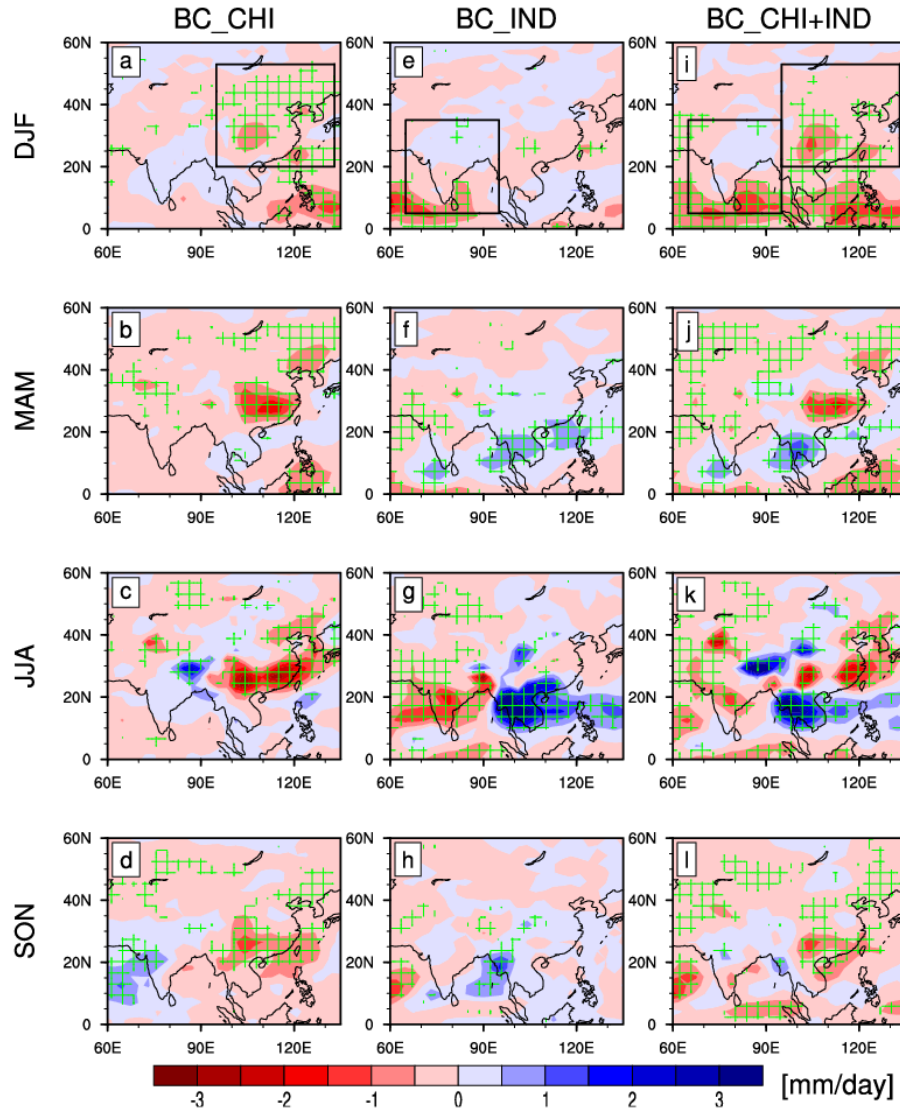
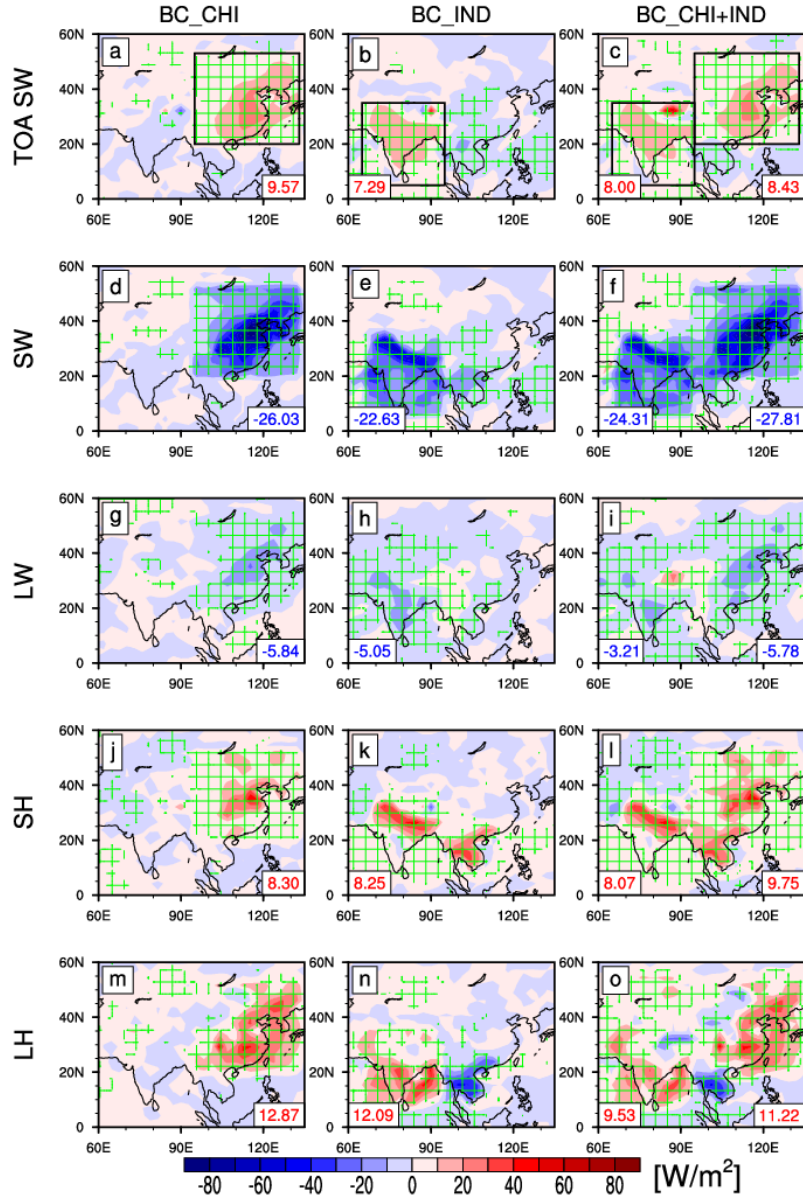
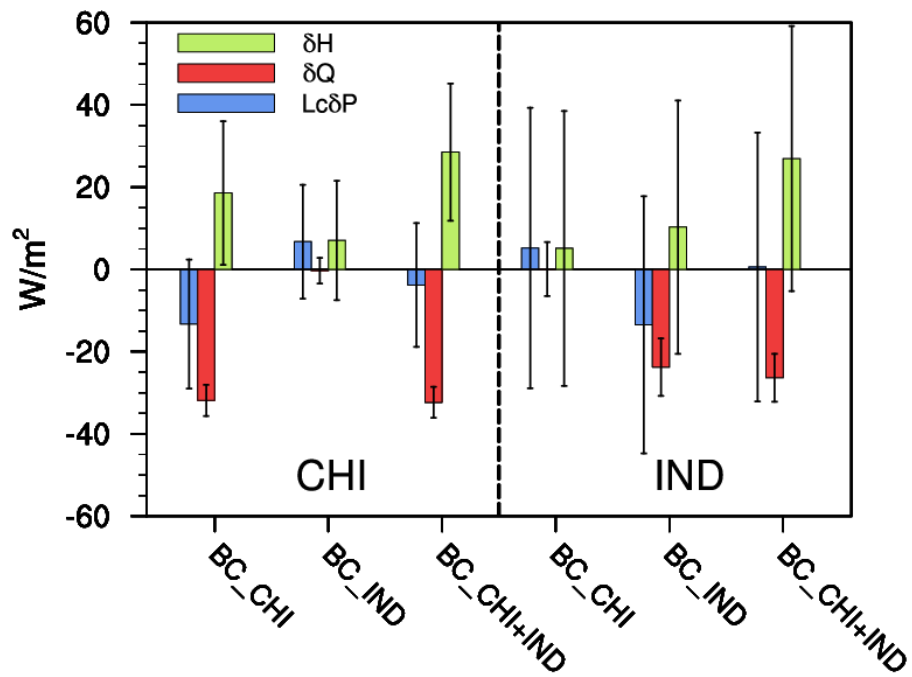


Figure 5. Spatial patterns of precipitation responses in (a-d) BC_CHI, (e-h) BC_IND, and (i-l) BC_CHI+IND for four seasons. The green gridlines indicate the regions where the responses are statistically significant above 95% level based on a two-tailed Student's t-test. The black boxes in (a), (e) and (i) highlight the region where BC aerosols are perturbed. Unit: mm/day



870

871 **Figure 6.** Spatial patterns of net TOA and surface energy responses in summer in
872 BC_CHI, BC_IND, and BC_CHI+IND, respectively. (a-c) TOA SW, (d-f) surface SW,
873 (g-i) surface LW, (j-l) surface SH, and (m-o) surface LH. Positive values mean
874 downward for radiation and flux changes. Area-averaged values over East China and
875 India are given in the lower right corners and lower left corners, respectively. The green
876 gridlines indicate the regions where the responses are statistically significant above 95%
877 level based on a two-tailed Student's t-test. The black squares highlight the regions
878 where BC are perturbed. Units: W/m^2



879

880 **Figure 7.** Summer area-averaged responses of the atmospheric energy budget terms
 881 over East China (CHI: 95°E-133°E, 20°N-53°N) and India (IND: 65°E-95°E, 5°N-
 882 35°N) in BC_CHI, BC_IND, and BC_CHI+IND. Error bars represent ± 1 standard
 883 deviations of the response. Unit: W/m^2

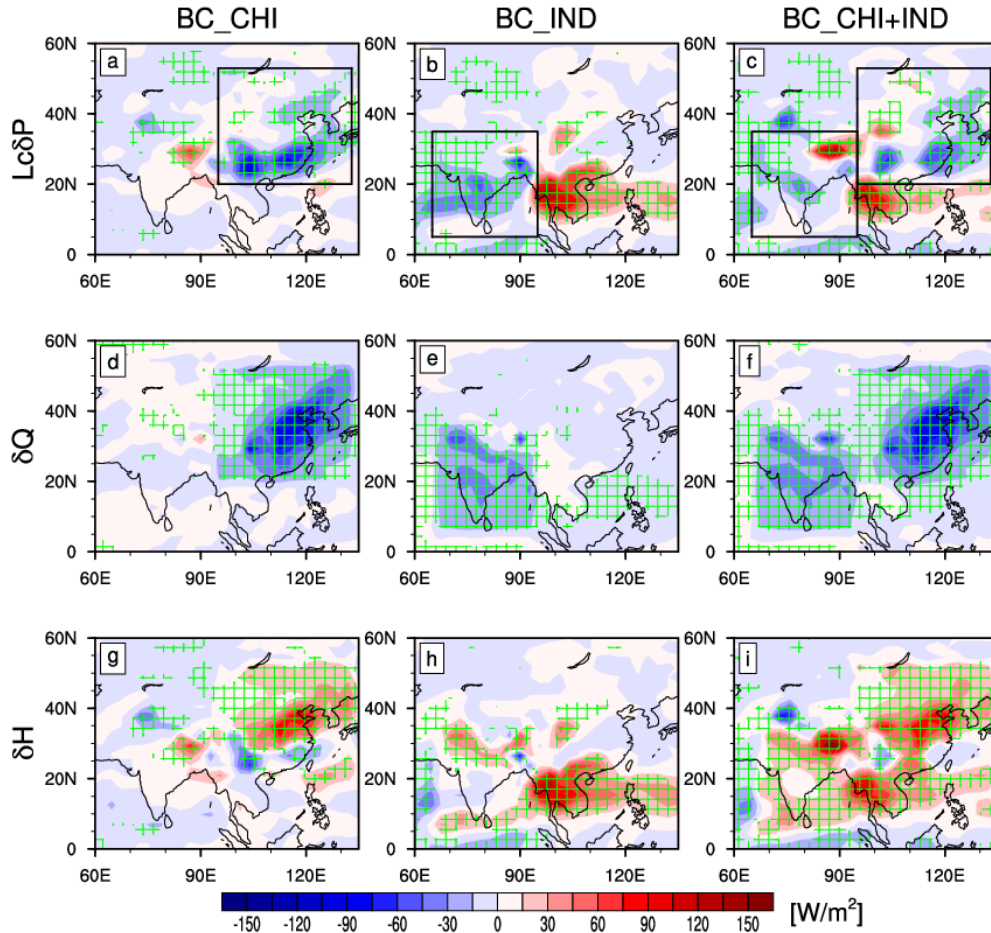


Figure 8. Summer spatial patterns of responses of the atmospheric energy budget terms in BC_CHI, BC_IND, and BC_CHI+IND. (a-c) $L_c\delta P$, (d-f) δQ and (g-i) δH . The green gridlines indicate the regions where the responses are statistically significant above 95% level based on a two-tailed Student's t-test. The black squares highlight the regions where BC are perturbed. Unit: W/m^2

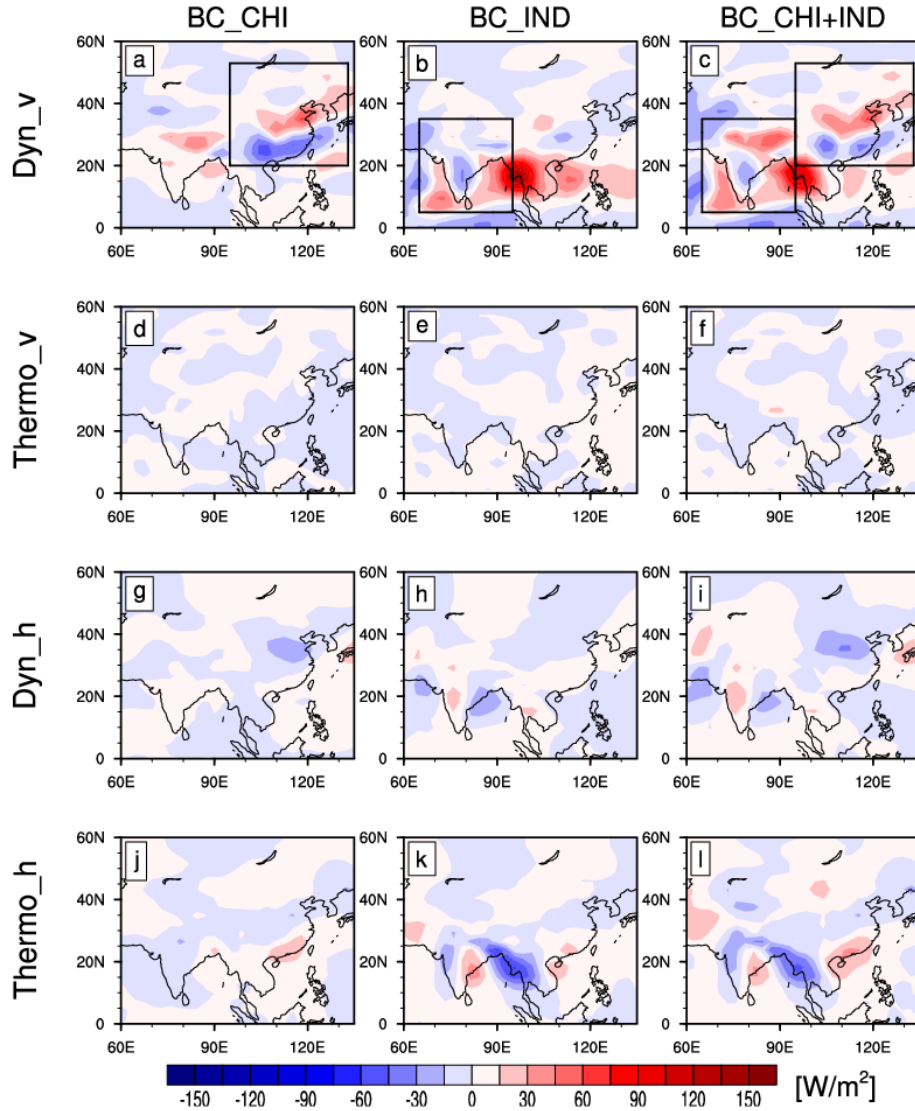


Figure 9. Summer spatial patterns of responses in the four terms decomposed by ΔH_m in BC_CHI, BC_IND, and BC_CHI+IND. (a-c) the dynamic components with changes in vertical atmospheric circulations (δH_{Dyn_v}), (d-f) the thermodynamic components with changes in vertical atmospheric circulations (δH_{Thermo_v}), (g-i) dynamic components with changes in horizontal DSE gradients (δH_{Dyn_h}), and (j-l) thermodynamic components with changes in horizontal DSE gradients (δH_{Thermo_h}). The black squares highlight the regions where BC are perturbed. Unit: W/m^2

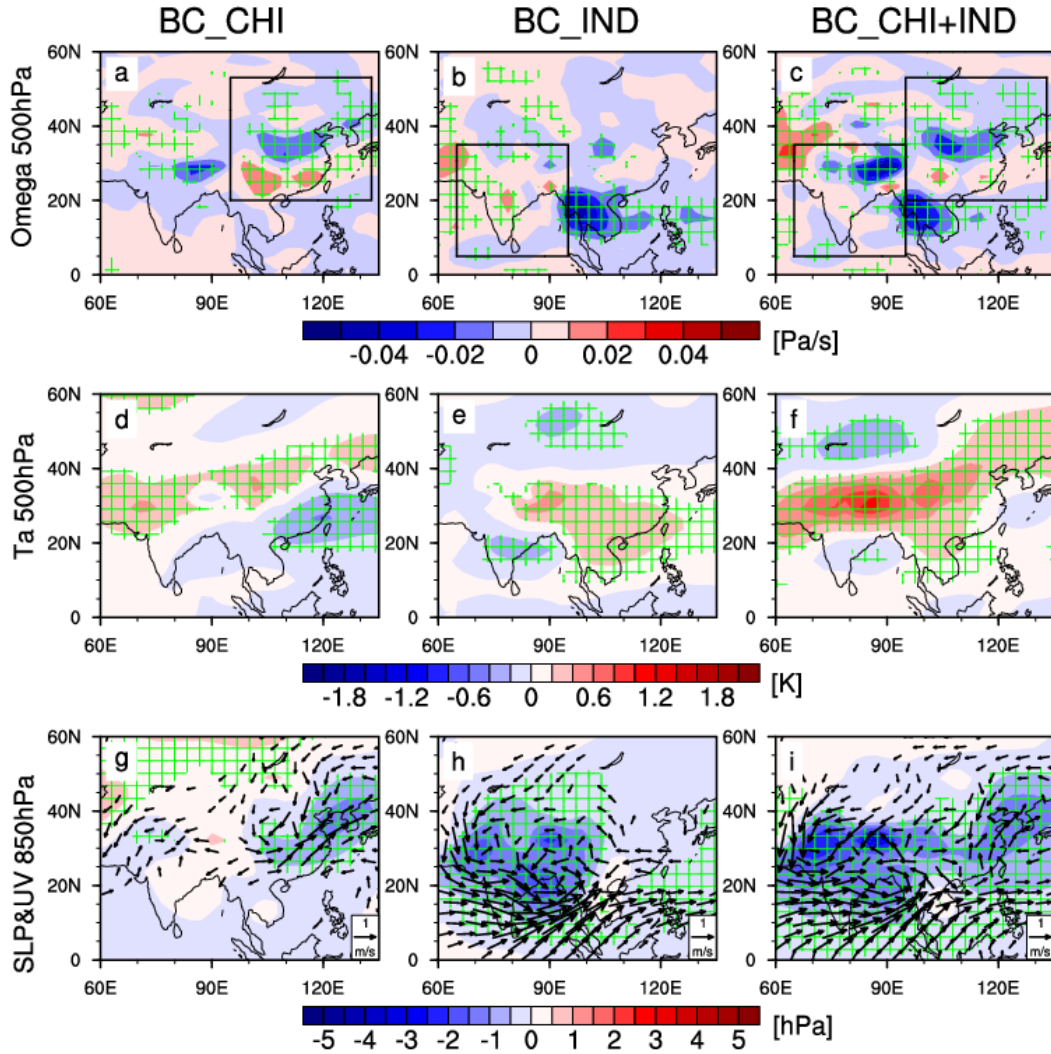


Figure 10. Summer spatial patterns of responses in (a-c) Omega at 500 hPa (Unit: Pa/s), (d-f) Ta at 500 hPa (Unit: K), and (g-i) SLP (Unit: hPa) and horizontal wind at 850 hPa (Unit: m/s) in BC_CHI, BC_IND and BC_CHI+IND. The green gridlines indicate the regions where the responses are statistically significant above 95% level based on a two-tailed Student's t-test. Wind vectors are only shown for grid boxes where at least one component of the wind significant above the 95% level are shown. The black squares highlight the regions where BC are perturbed.

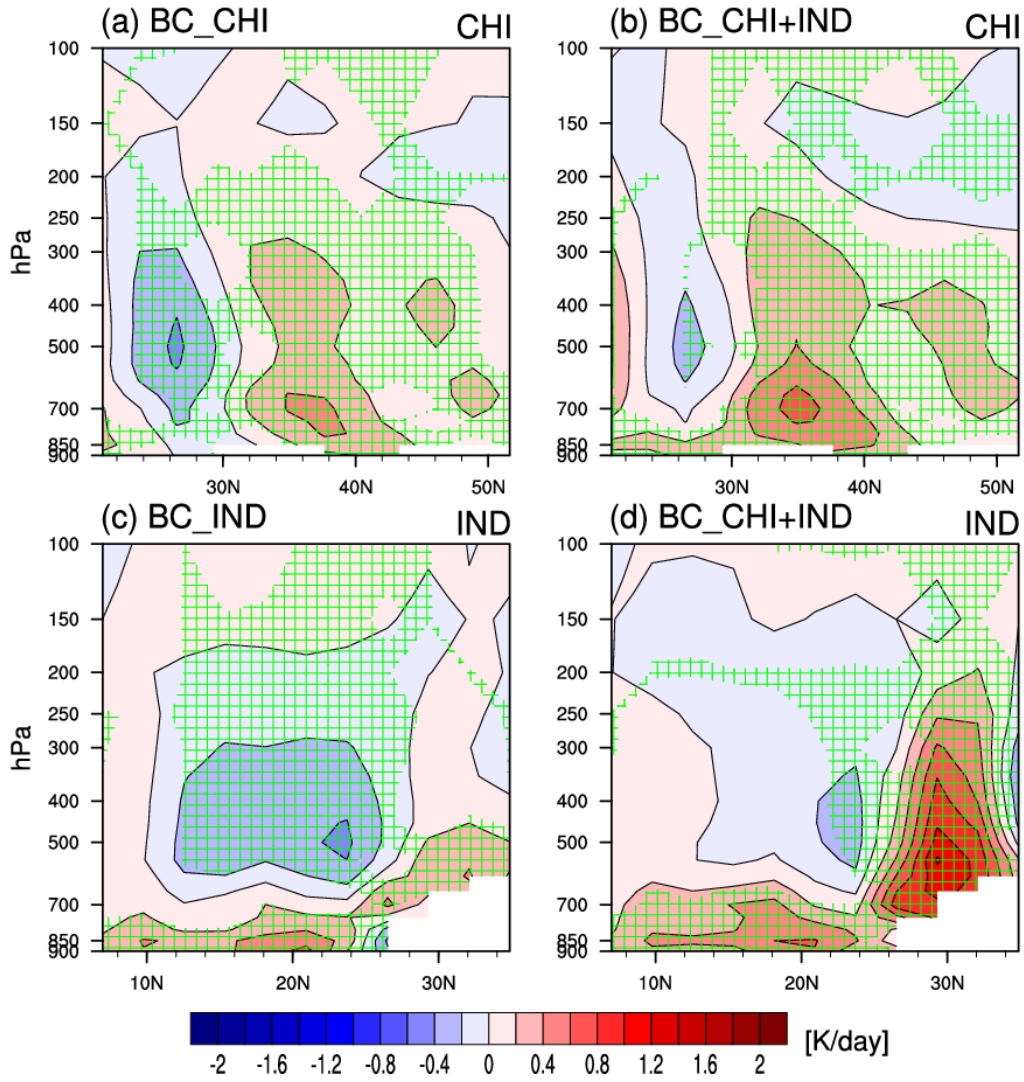


Figure 11. Zonal mean of diabatic heating responses averaged over (a-b) East China (95°E-133°E, the black square in Fig.10a) for BC_CHI and BC_CHI+IND, and over (c-d) India (65°E-95°E, the black square in Fig.10b) for BC_IND and BC_CHI+IND in summer. The green gridlines indicate the regions where the responses are statistically significant above 95% level based on a two-tailed Student's t-test. The white part indicates a symbol of topography. Unit: K/day

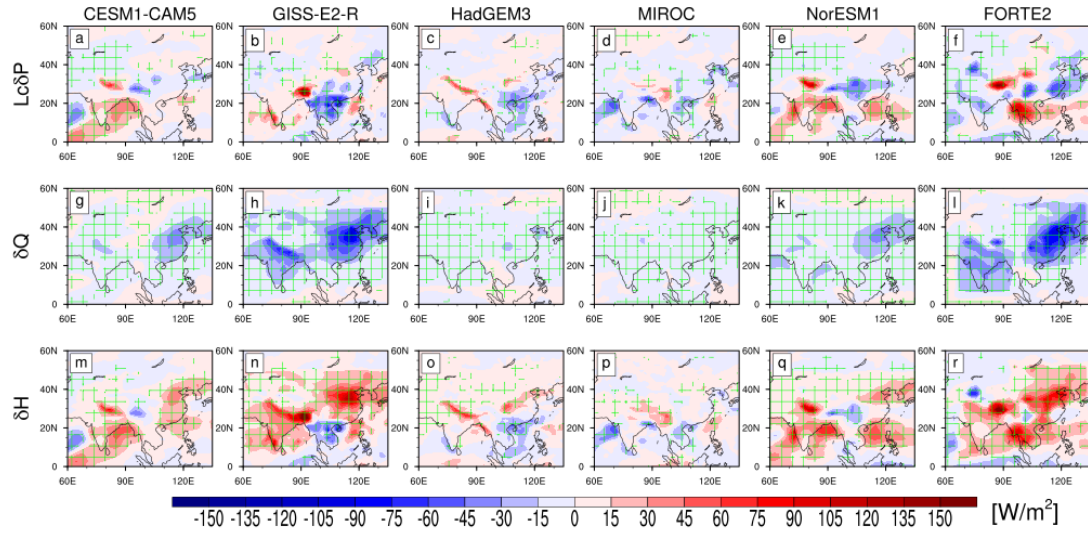
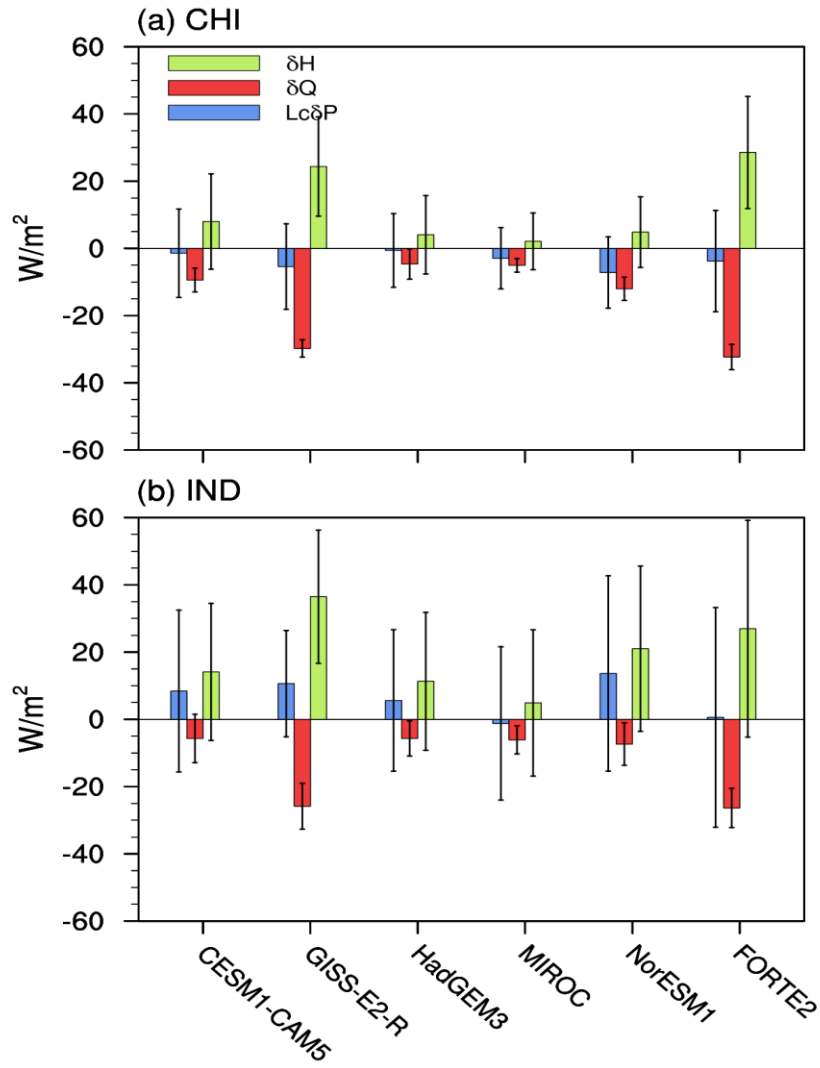


Figure 12. Summer spatial patterns of responses of the atmospheric energy budget terms in the five PDRMIP models and the BC_CHI+IND simulation in FORTE2. (a-e) $L_c\delta P$, (f-j) δQ and (k-o) δH . The green gridlines indicate the regions where the responses are statistically significant above 95% level based on a two-tailed Student's t-test. Unit: W/m^2



920

921 **Figure 13.** Summer area-averaged responses of the atmospheric energy budget terms
 922 over (a) East China (CHI: 95°E-133°E, 20°N-53°N) and (b) India (IND: 65°E-95°E,
 923 5°N-35°N) in the five PDRMIP models and the BC_CHI+IND simulation in FORTE2.
 924 Error bars represent ± 1 standard deviations of the response. Unit: W/m^2